

Long-term effects of anthropogenic CO₂ emissions simulated with a complex earth system model

Uwe Mikolajewicz · Matthias Gröger · Ernst Maier-Reimer ·
Guy Schurgers · Miren Vizcaíno · Arne M. E. Winguth

Received: 15 February 2006 / Accepted: 18 September 2006
© Springer-Verlag 2006

Abstract A new complex earth system model consisting of an atmospheric general circulation model, an ocean general circulation model, a three-dimensional ice sheet model, a marine biogeochemistry model, and a dynamic vegetation model was used to study the long-term response to anthropogenic carbon emissions. The prescribed emissions follow estimates of past emissions for the period 1751–2000 and standard IPCC emission scenarios up to the year 2100. After 2100, an exponential decrease of the emissions was assumed. For each of the scenarios, a small ensemble of simulations was carried out. The North Atlantic overturning collapsed in the high emission scenario (A2) simulations. In the low emission scenario (B1), only a temporary weakening of the deep water formation in the North Atlantic is predicted. The moderate emission scenario (A1B) brings the system close to its bifurcation point, with three out of five runs leading to a

collapsed North Atlantic overturning circulation. The atmospheric moisture transport predominantly contributes to the collapse of the deep water formation. In the simulations with collapsed deep water formation in the North Atlantic a substantial cooling over parts of the North Atlantic is simulated. Anthropogenic climate change substantially reduces the ability of land and ocean to sequester anthropogenic carbon. The simulated effect of a collapse of the deep water formation in the North Atlantic on the atmospheric CO₂ concentration turned out to be relatively small. The volume of the Greenland ice sheet is reduced, but its contribution to global mean sea level is almost counterbalanced by the growth of the Antarctic ice sheet due to enhanced snowfall. The modifications of the high latitude freshwater input due to the simulated changes in mass balance of the ice sheet are one order of magnitude smaller than the changes due to atmospheric moisture transport. After the year 3000, the global mean surface temperature is predicted to be almost constant due to the compensating effects of decreasing atmospheric CO₂ concentrations due to oceanic uptake and delayed response to increasing atmospheric CO₂ concentrations before.

U. Mikolajewicz (✉) · M. Gröger · E. Maier-Reimer ·
G. Schurgers · M. Vizcaíno
Max-Planck-Institut für Meteorologie, Bundesstrasse 53,
20146 Hamburg, Germany
e-mail: uwe.mikolajewicz@zmaw.de

Present Address:

G. Schurgers
Department of Physical Geography and Ecosystem
Analysis, Lund University, Lund, Sweden

Present Address:

M. Vizcaíno
Department of Geography and Center for Atmospheric
Sciences, University of California, Berkeley, CA, USA

A. M. E. Winguth
Department of Atmospheric and Oceanic Sciences,
Center for Climatic Research, Madison, USA

1 Introduction

The prediction of the climate changes to be expected within the remainder of this century as a consequence of anthropogenic emissions of greenhouse gases has been one of the most important research activities in atmospheric and oceanic sciences of the last two dec-

ades. Almost all state-of-the-art climate models have been applied to simulate the climate changes up to the year 2100, which are coordinated by the IPCC (Intergovernmental Panel on Climate Change, Houghton et al. 2001). In contrast to the IPCC-type simulations, this paper focuses on centennial to millennial time scale changes in the earth system. The assessment of climate changes on millennial time scales requires a consideration of major components of the earth system typically not represented in the IPCC-type simulations (e.g. ice sheets, marine sediments) and a computationally less expensive model.

The goal of this paper is to investigate potential long-term changes in the earth system caused by anthropogenic emissions with a complex earth system model (ESM), with a special focus on feedbacks between different physical and biogeochemical components within the next 1,000 years.

In a number of studies, the long-term equilibration of atmosphere-ocean models to elevated levels of CO₂ has been investigated (e.g. Manabe and Stouffer 1994; Voss and Mikolajewicz 2001a), reporting an—at least temporarily—strongly reduced ventilation of the deep ocean and substantial changes in ocean heat transport. Studies with earth system models focussing on millennia and longer time scales have been so far (to our knowledge) only performed with earth system models of intermediate complexity (EMICs, an overview is given in Petoukhov et al. 2005). In this type of models, major simplifications have been made in comparison with general circulation models. In coupled atmosphere–ocean models, the atmospheric component is by far the most expensive contribution, and all earth system models of reduced complexity have used a simpler and computationally much less expensive representation of the atmosphere. For example, the UVic model (Weaver et al. 2001) uses an energy balance model of the atmosphere and the CLIMBER-2 model (Petoukhov et al. 2000) uses a highly parameterised representation of the atmosphere with very coarse resolution. Here, we will introduce an earth system model that utilises an—albeit coarse resolution—atmospheric general circulation model. Changes in the hydrological cycle will play an important role for future climate changes, especially for changes in the thermohaline circulation of the ocean (e.g. Stouffer et al. 1989; Dixon et al. 1999; Mikolajewicz and Voss 2000; Gregory et al. 2005). Thus, an atmospheric general circulation model (GCM) yields a more realistic prediction of future changes in the hydrological cycle than atmospheric components used in EMICs. The computational cost of our earth system model is substantially reduced by the application of a periodically

synchronous coupling technique. The physical part of the model consists of an atmospheric and oceanic GCM with a simple dynamic/thermodynamic sea ice component and a three-dimensional thermomechanical ice sheet model. The biogeochemical model components involve a dynamic vegetation model and a marine biogeochemistry model.

The outline of the paper is as follows: the earth system model and the coupling between its components are introduced in Sect. 2. For some key parameters, the simulated climate is compared with observations. In Sect. 3, experiments with three different prescribed anthropogenic CO₂ emission scenarios are described. The changes in atmosphere, ocean, ice sheets, and the marine and terrestrial carbon cycle are investigated and feedbacks between the different compartments are analysed. However, due to the complexity of the model, not all results can be described in detail in a single paper. So the idea is to give an overview of the most relevant results in this paper and leave a more in-depth going analysis of specific aspects to a series of future papers (Schurgers 2006; Vizcaíno 2006). In Sect. 4, the summary and conclusion of this paper are given.

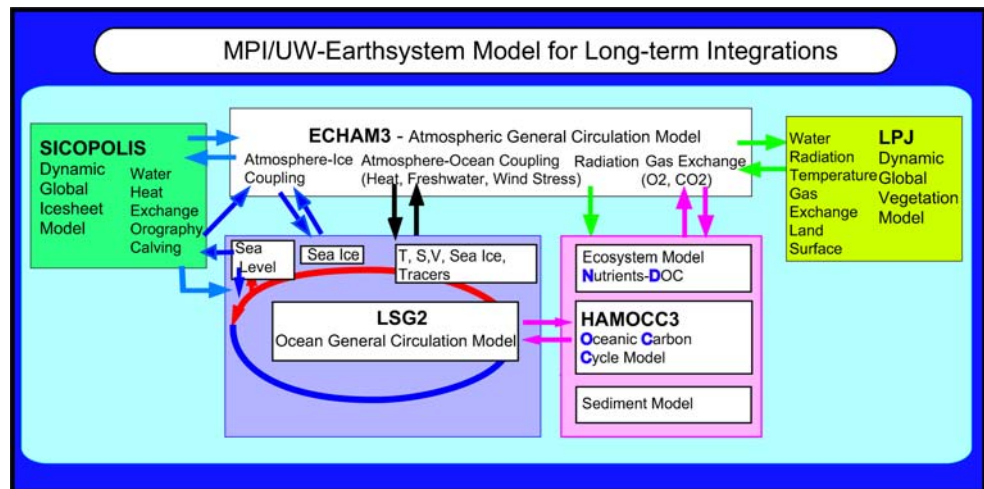
2 The earth system model

2.1 Model description

The physical core of the earth system model consists of the atmospheric GCM ECHAM3 (Roeckner et al. 1992) and the ocean GCM LSG2 (Maier-Reimer et al. 1993). Additional components of the model are the three-dimensional thermomechanical ice sheet model SICOPOLIS (Greve 1997), the marine carbon cycle model HAMOCC3 (Maier-Reimer 1993), and the dynamical global vegetation model LPJ (Sitch et al. 2003). In this paper, only an overview over the coupling of the ice sheet and terrestrial vegetation to the other components will be given. More details will be given elsewhere (Schurgers 2006; Vizcaíno 2006). A schematic diagram of the model is shown in Fig. 1.

The spectral atmospheric GCM ECHAM3.6 (Roeckner et al. 1992) has a T21 resolution (roughly 5.6° in grid point space) with 19 vertical layers. The prognostic variables are vorticity, divergence, temperature, humidity, surface pressure, and cloud water. The annual and diurnal cycles of the solar irradiance are included. The model time step is 40 min.

The ocean model LSG2, an improved version of the LSG-model (Maier-Reimer et al. 1993), is used with a horizontal resolution of 5.6° on two overlapping grids

Fig. 1 Schematic description of the earth system model

(64×64 grid points on an Arakawa E grid). The model uses the standard set of approximations in hydrostatic ocean models (Boussinesq, incompressibility). The advection of momentum has been neglected in the momentum equations. The thickness of the 22 vertical levels varies with depth (50 m in the top layer to almost 800 m at 5,600 m depth). The model has a mass flux surface boundary condition for salinity and the thickness of the uppermost model level depends on the time-varying sea level. The thickness of the bottom cell is variable, thus allowing a smooth representation of the topography. Due to the fully implicit formulation of the model equations, the model can be run with a time step of 1 month. In order to resolve more of the short-term variability, a time step of 5 days was chosen for the model. The thermodynamics of the surface layer are calculated with a time step of 1 day in order to give a consistent response to the atmospheric forcing.

Several state-of-the-art sub-grid-scale parameterisations have been implemented in the LSG2 model, which were not included in the original LSG model (Maier-Reimer et al. 1993). This includes the Gent et al. (1995) parameterisation of the eddy induced tracer transport with interactive calculation of the coefficient (Visbeck et al. 1997). Vertical diffusivities in the interior are Richardson number dependent (Pacanowski and Philander 1981). To account for the wind induced stirring at the surface a simple parameterisation is used: The input of energy is proportional to the cube of the wind speed at 10 m height and decays exponentially with depth. The penetration depth is reduced in case of stable stratification. To better account for the contribution of dense shelf waters to the ventilation of the deep ocean, a simple parameterisation of slope convection is included: Water on the

bottom of a grid cell may also continue to convect on a neighbouring grid point, if this grid point is deeper and if the water mass stratification is unstable. The sub-grid-scale parameterisations and their respective parameter values are based on the set of parameterisations implemented in the MPI-OM ocean GCM (Marsland et al. 2003).

The advection of tracers is discretised using a second order total variation diminishing scheme (Sweby 1984). This scheme shows considerably smaller numerical diffusion compared to the first order upwind advection scheme in the original LSG, but almost without producing the spurious oscillations typical for the classical second order central differences scheme. Overshooting is minimised using flux limiters derived from the ratio between the first and second derivative.

The ocean model includes a simple dynamic sea ice model. The advection velocity is the sum of the velocity of the uppermost ocean layer and a wind-derived component (2% of the wind velocity with geostrophic rotation of 19°). The advection of sea ice is discretised with a first order upwind scheme. The piling up of sea ice at coasts by steady onshore winds is kept small by a diffusive term with a horizontal diffusion constant of $2,000 \text{ m}^2/\text{s}$.

A simple water conserving runoff model is included in the ocean model. A constant bucket depth of 50 cm is used everywhere. The time dependent transport direction is determined using the direction of the strongest topography gradient. Topography in the model can change due to changes in ice sheet thickness and isostatic rebound in response to former ice loads. As the land–sea mask was derived from the atmosphere model, some ocean points on the Arakawa E grid do not have at least one adjacent ‘wet’ velocity point (the necessary condition for a wet velocity point

being that all four neighbouring scalar points need to be wet). These grid points are treated as isolated lakes with a constant depth of 50 m. North and South America are connected by a barrier, Bering Strait is open.

The coupling time step between atmosphere and ocean is 1 day. The ocean delivers distributions of sea surface temperature (SST) and sea ice, whereas the atmosphere supplies fluxes of heat, momentum and mass (water).

The three-dimensional dynamic/thermodynamic ice sheet model SICOPOLIS (Greve 1997) is based on the shallow-ice approximation (longitudinal stress gradients are neglected). It includes a formulation of isostasy. A simple parameterisation of calving is included in the model. For the experiments described later, a horizontal resolution of 80 km has been chosen, and a vertical resolution of 21 layers in the ice and 11 in the lithosphere. The model is forced with surface temperatures, mass balance, geothermal heat flux, and sea level changes. For the calculation of melting rates, a degree-day method has been applied (Reeh 1991), where the melting is proportional to positive (on the Celsius scale) near-surface air temperatures. The snowfall rates are calculated from seasonal precipitation rates, converted into solid precipitation using the near-surface air temperatures. The ice sheet model SICOPOLIS is coupled to the other compartments of the earth system model, supplying modifications of the freshwater flux for the ocean/runoff model, of the glacier mask for atmosphere and vegetation models, and of the orography for the atmosphere and runoff model. Details are given in Vizcaíno (2006).

Our earth system model includes an interactive carbon cycle consisting of the marine biogeochemistry model HAMOCC3 and the dynamic vegetation model LPJ, which also supplies surface properties for the atmospheric GCM ECHAM. Details of this coupling are presented in Schurgers (2006). The prognostic atmospheric CO₂ concentration is used for radiation calculations in the atmosphere component of the ESM.

The dynamic global vegetation model LPJ (Sitch et al. 2003) simulates the spatial distribution of ten plant functional types (PFTs) over the earth, and within each PFT four living biomass and three litter carbon pools are defined. A grid cell can contain more than one PFT, and has two common soil carbon pools. For each PFT, photosynthesis (described according to Farquhar et al. 1980) and autotrophic and heterotrophic respiration are the main processes determining the carbon fluxes. Besides that, establishment and mortality are modelled explicitly, as well as the phenology changes over the year. The model calculates

surface properties of the land points such as background albedo, vegetation cover, and roughness length which are then used in the atmosphere model ECHAM3. The model has an identical resolution to the atmosphere model. The model fluxes of carbon are used in the calculation of the atmospheric CO₂ concentration. The time step for the coupling of ice sheet and terrestrial vegetation with the other components is 1 year.

The marine carbon cycle model applied in this study is basically the HAMOCC3 model (Maier-Reimer 1993; Winguth et al. 1994). The tracer fields are advected within the LSG2 model using the identical advection scheme as for temperature and salinity. Temperature, salinity, and sea ice fields for the calculation of biogeochemistry are taken from the ocean model, incoming shortwave radiation and wind speed from the atmosphere model. The atmospheric CO₂ partial pressure and vertical gradients of carbon are linked with three pumping mechanisms (Volk and Hoffert 1985): The solubility pump with high solubility at low temperatures, and two biological pumps, which are the dominating “soft tissue pump” caused by the formation of organic material and depletion of nutrients and carbon in the surface water and the counteracting CaCO₃ pump. Phosphate (PO₄) is treated as the only nutrient-limiting tracer for photosynthesis in order to avoid the complication arising from denitrification and N fixation. Export production (EP), the amount of primary production transported from the euphotic zone into deeper layers is parameterised by the availability of light, temperature T (in °C), nutrients (PO₄), and vertical mixing v :

$$EP = r(T, L) \frac{50 \text{ m } PO_4^2}{v PO_4 + P_0} \quad (1)$$

with a growth rate $r(T, L)$ following a formula of Smith (1936). The temperature dependence follows Eppley (1972). The light function $g(L) = 0.005 L_{sw}$ uses the downward shortwave radiation L_{sw} from ECHAM3. $P_0 = 0.02 \text{ mmol m}^{-3}$ is the nutrient half saturation constant. Production of opal forming species is simulated as function of EP and silica availability, and CaCO₃ production is controlled by export production EP, the competing opal production, and by a temperature (T) dependent formulation $a/(1+a)$ with $a = \exp(0.1^\circ\text{C}^{-1}(T-10^\circ\text{C}))$.

Remineralisation of particulate organic carbon (POC) is modelled according to a temperature and oxygen dependent formulation. At the sea floor, the carbon and silica budget is closed with a single layer sediment module for opal, CaCO₃ and POC. Model

parameters have been optimised in order to reduce the long-term drift, so that the accumulation of sediments for the reference run is in near-equilibrium with input from continental weathering. The assumption is made that weathering rates, which are calculated from the spin up integration, are to be constant for the time scales of interest and do not depend strongly on climate, but the sedimentation rates do change with climate. Ocean biogeochemistry is calculated once per month.

For very long integrations the model is, despite its coarse resolution, still computationally very expensive. More than 90% of the computer time is consumed by the atmosphere model. On time scales longer than decades, the memory of the physical system resides in the slower components such as ocean and ice sheets, whereas the long-term memory of the atmosphere is rather small. Voss and Sausen (1996) have made use of this and introduced the periodically-synchronous coupling technique for atmosphere–ocean GCMs and demonstrated that it works properly for problems with long timescales (Voss et al. 1998). This approach has been applied on various problems, e.g. for long-term response to increased atmospheric CO₂ levels (Voss and Mikolajewicz 2001a), the effect of melt water input on climate (Schiller et al. 1997; Mikolajewicz et al. 1997) and for the effect of insolation changes on climate (Voss and Mikolajewicz 2001b).

The technique, as suggested by Voss and Sausen (1996), is based on alternating periods of fully synchronous integrations and periods where the ocean is driven in stand-alone mode by fluxes from previous synchronous integration periods. Voss et al. (1998) used 15 months of synchronous integrations and 48 months of ocean-only simulations. With this periodically-synchronous coupling, they achieved a reduction of the consumed computer time by a factor of three compared to the fully synchronously coupled model. Our attempts to obtain an even larger speed-up by longer ocean-only simulations led to problems at the ice edge with the build up of unrealistically thick sea ice caused by the strong non-linearity in air–sea heat flux at the ice edge. For the original choice of parameters this effect is small, but it grows rapidly for longer flux-only periods. For example, the oceanic heat loss in winter can easily reach up to 1,000 W/m² in grid points with deep convection close to the sea ice edge, but is substantially smaller in the presence of sea ice. If during the synchronous period a grid point with cold winds blowing from ice covered areas is kept ice-free due to deep convection, the convection can shift location in the ocean-only periods. Suppressed convection in combination with the prescribed strong heat loss

then leads to an unrealistic build up of sea ice. In a fully coupled simulation the presence of sea ice would reduce the air–sea heat exchange drastically and the cold air would reach the next ocean grid point downstream, where it either would initiate convection or ultimately lead to the formation of sea ice.

The simplest model capturing this type of behaviour is a two-dimensional energy balance model. This model is formulated here as non-linear anomaly model. The model simulations now consist of alternating periods of the fully coupled model (2 years in the experiments described in this paper) and of periods where all models but the AGCM get their forcing from previously calculated synchronous forcing periods, but where the heat fluxes for the ocean are adapted to the actual state of the surface ocean (incl. sea ice) using the non-linear EBM. For part of the simulations the length of the simulation with atmospheric GCM is calculated during the run depending on the degree of changes in the surface ocean properties. A description of the modifications in the periodically-synchronous coupling technique can be found in Appendix 1. This method has been validated by repeating simulations with a fully synchronously coupled model (see Appendix 2).

2.2 Initialisation and control climate of the model

Starting from a previous model state, the model has been run for more than 10,000 years with basically the same unchanged parameters as in the experiments. During this spin up simulation the flux corrections for the ice sheet model have been calculated.

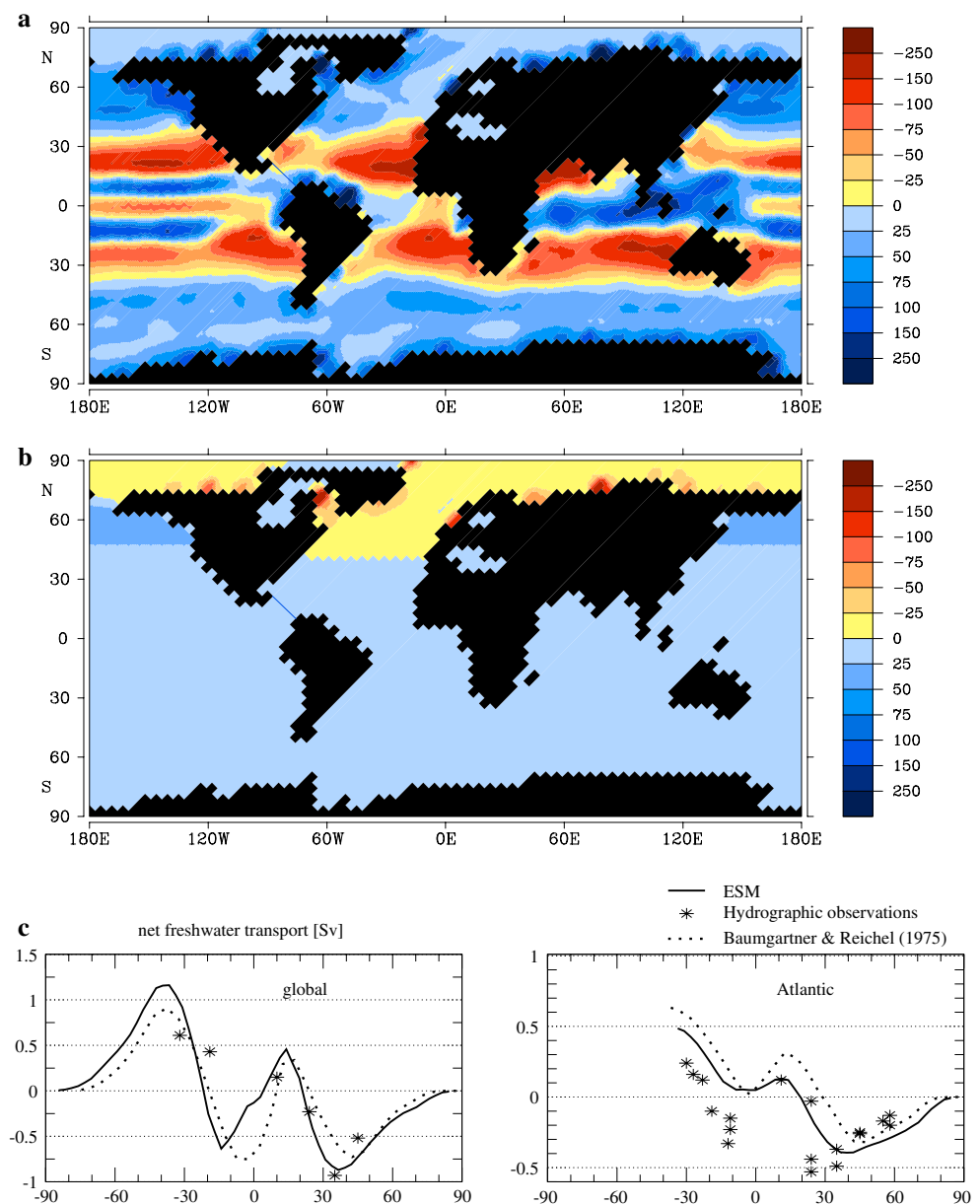
The atmosphere–ocean dynamical core of the ESM runs with two flux corrections: an artificial freshwater export from the North Atlantic/Arctic to the North Pacific of 0.14 Sv and an additional easterly wind stress in the tropical oceans. The additional freshwater export improves the state of the model substantially, especially its representation of the Atlantic overturning circulation and oceanic heat transport. Due to its coarse resolution and the only partially resolved synoptic variability, the atmospheric model produces too strong a convergence of atmospheric moisture transports within the Arctic and the adjacent land areas. A freshwater input of 0.4 Sv north of 60°N into the Atlantic and the Arctic is simulated. This is clearly above climatological estimates. Baumgartner and Reichel (1975) give a value of 0.19 Sv. The simulated runoff from Siberian rivers is 0.1 Sv, which is rather realistic. The simulated runoff from North America into the Hudson Bay and into the Labrador Sea is of similar magnitude, caused by too high precipitation over the north eastern US and Canada. The precipi-

tation in the northeast Atlantic is overestimated as well. The value of 0.14 Sv is motivated by keeping the flux correction as small as possible and to maintain a reasonable realistic ocean climate. For each day, the sum of the positive net freshwater fluxes into the ocean is calculated and a multiplicative factor (<1) determined, which is applied for positive values only in order to avoid changes of the sign of the actual net freshwater flux. In order to keep the impact on the latitudinal distribution of moisture as small as possible, the freshwater is exported to the North Pacific and added uniformly there. A plot of the resulting freshwater flux correction together with the total net

freshwater flux into the ocean is shown in Fig. 2. The freshwater input into the northern North Atlantic and the Arctic is—in spite of the applied flux correction—somewhat larger than the climatological values. The simulated atmospheric freshwater fluxes in the other parts of the ocean lie within the uncertainty spanned by different climatological estimates (Fig. 2c).

The second correction, the wind-stress correction, is designed to improve the representation of the climate in the tropics, especially the position of the intertropical convergence zone (ITCZ). Without any wind stress correction, the model ended up in a state with a permanent El Niño and almost vanishing east–west SST

Fig. 2 **a** Net freshwater forcing for the ocean model in millimetre per month. *Positive values* indicate flux into the ocean. **b** Applied flux correction in millimetre per month. **c** Resulting northward freshwater transport of the ocean in Sv together with observational estimates. Hydrographic observations according to Wijffels (2001) and references therein



gradient in the Pacific. The wind stress correction τ_{corr} has been calculated with the following formulas:

$$\begin{aligned}\tau_{\text{xcorr}} &= \tau_0 \exp(-0.5\phi^2), \\ \tau_{\text{ycorr}} &= \tau_0(\phi/1.4) \exp(-0.5\phi^2),\end{aligned}\quad (2)$$

where τ_0 is the amplitude (–15 mPa), and ϕ is the latitude in degrees. The zonal component is additionally reduced for the next two grid points west of land points. The resulting correction pattern is shown in Fig. 3b. In the tropics it mimics the effect of trade winds; in high latitudes it is negligible. In comparison to the mean momentum flux (see Fig. 3a), the size of the flux correction is rather small. Between atmosphere and ocean, no other flux corrections are applied. The air–sea heat flux is not adjusted at all, thus avoiding distortion in the non-linear dependence of heat fluxes on SST and sea ice.

A flux correction has been applied for the interface between atmosphere and ice sheets. The ice sheet model is forced with anomalies of ECHAM3 relative to the climate of the control run added to the ERA–40 climatology (Gibson et al. 1997). This applies for the seasonal 2-m temperatures and the precipitation rates.

For the initialisation of the ice sheets, the ERA-40 climatology plus a time-dependent signal from the ice cores of GRIP and Vostok has been used as atmospheric forcing during two glacial cycles. Details of this spin up are discussed in Vizcaíno (2004).

In the following, the climate of the earth system model is discussed. The model climate is derived from a 2,250 year mean of the control run without anthropogenic forcing with a mean atmospheric CO₂ concentration of 279.5 ppm.

The zonal mean of atmospheric near surface temperature is shown in Fig. 4a. The model’s simulated climate has a cold bias in comparison to observations in high latitudes and a warm bias in low latitudes. Especially in northern hemisphere winter, the model’s climate is 10 K colder over the Arctic. This bias is related to the underestimation of wintertime clouds over the Arctic. In the southern hemisphere, the temperature errors are smaller and the simulated zonal mean surface air temperatures lie within the range spanned by different climatologies (Fig. 4a). The zonal mean precipitation is shown in Fig. 4b. In summer, the simulated precipitation over the Arctic is about twice as strong as in the observational estimates. The model underesti-

Fig. 3 **a** Long-term mean wind stress forcing for the ocean. **b** Applied flux correction. Units are mPa. The amplitude of the wind stress is indicated by the colour, the direction by the arrows. No arrows are plotted for amplitudes smaller than 10 mPa

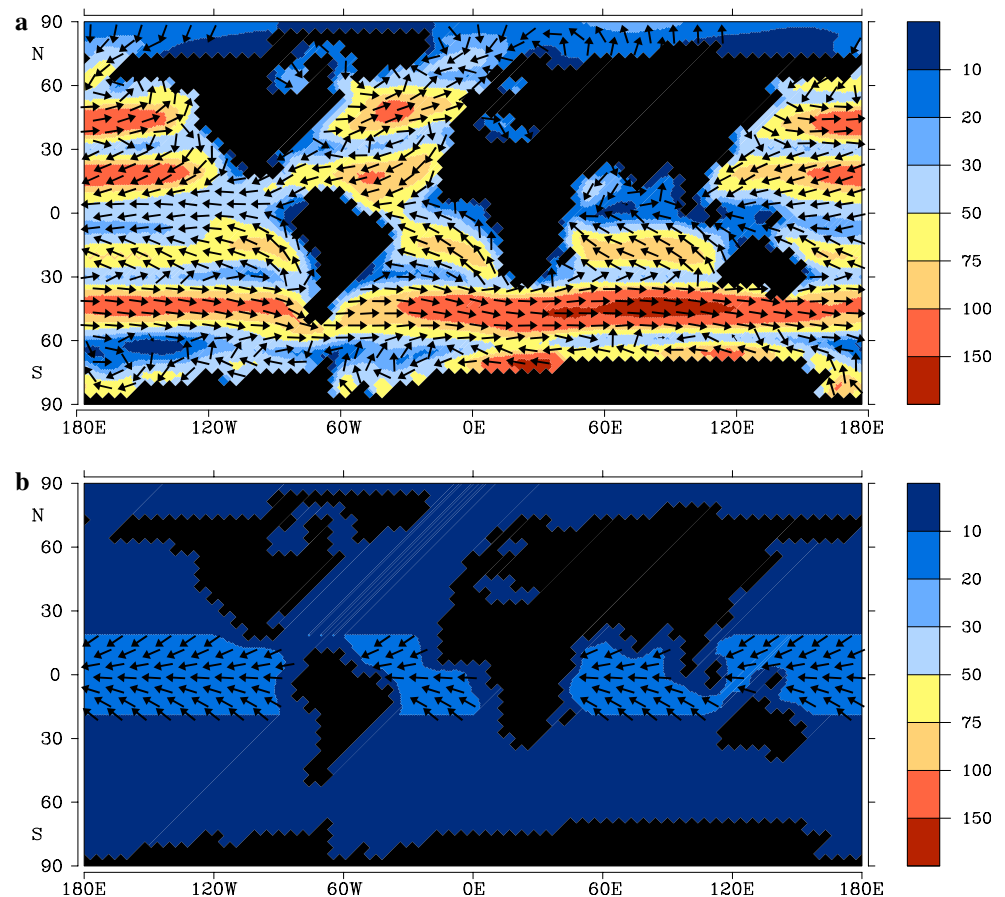
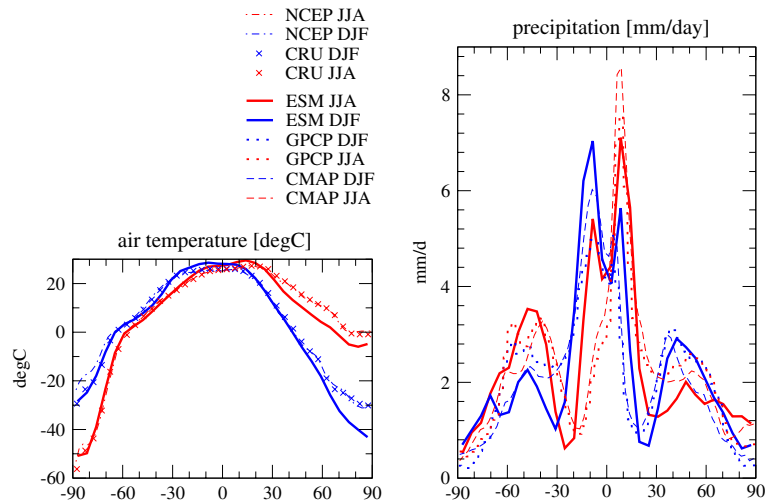


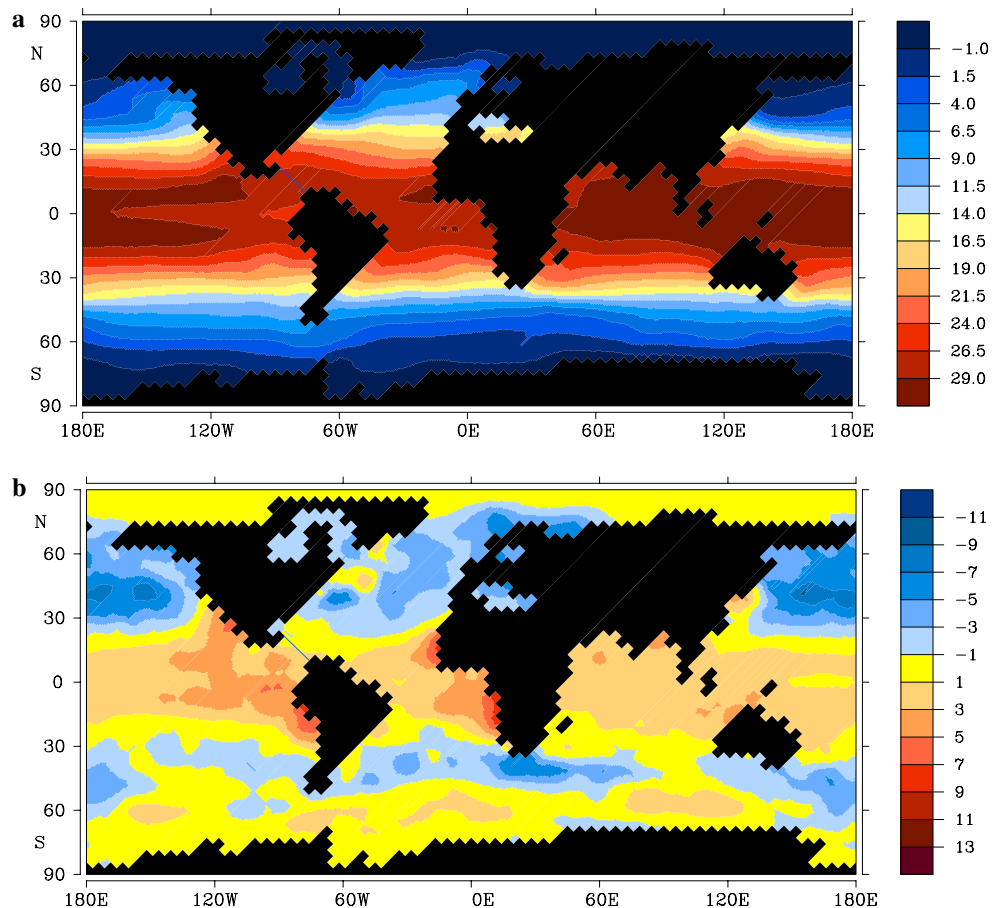
Fig. 4 Zonal mean near surface air temperature (*left*, in °C) and total precipitation (*right*, in mm/day) together with observations. *NCEP* Kalnay et al. 1996, *GPCP* Huffman et al. 1997, *CMAP* Xie and Arkin 1997, *CRU* Jones et al. 1999. Displayed are values for climatological summer (JJA) and winter (DJF)



mates in summer the latitudinal variations in the subtropics and strongly underestimates for all seasons the precipitation at mid latitudes. In the tropics the modelled precipitation lies within the band of observational estimates. Near the South Pole, the model overestimates precipitation as well.

In Fig. 5, the temperature of the uppermost level of the ocean model (covering the top 50 m) and the deviation from the WOCE global hydrographic climatology (WGHC, Gouretski and Koltermann 2004) is shown. The model overestimates the tropical SST by typically 1–2.5 K. In the coastal upwelling areas of the subtropics,

Fig. 5 a Climatological model SST (temperature of the uppermost level centred at 25 m depth) in °C. **b** Deviation from the WGHC climatology (Gouretski and Koltermann 2004) in K



simulated SSTs are too warm. This is a consequence of the underestimation of the stratocumulus clouds in the atmosphere model, a well-known problem in coupled atmosphere-ocean models (e.g. Chevallier et al. 2001). The resulting overestimation of the surface heating by solar radiation in the subtropical east Pacific and east Atlantic in combination with the difficulties of coarse resolution ocean models to represent the wind-driven coastal upwelling properly lead to an underestimation of the east–west temperature gradient at the equator. The resulting underestimation of the easterly winds at the equator leads to reduced upwelling and thus further amplifies the underestimation of the zonal temperature gradient. Due to this feedback, the flux correction of the wind stress turned out to be necessary. In mid-latitudes, the model simulates a too cold climate, typical errors are 3 K for the North Atlantic and 5 K for the North Pacific. In the Southern Ocean, the temperature error is relatively small.

The model reproduces the basic features of the near-surface salinity (see Fig. 6). In order to avoid confusion by model points that are treated as 50 m deep lakes (due to the lack of adjacent velocity points without the possibility to change the initial salinity), we show

salinity of the second model layer centred at 75 m depth. Comparison with the WGHC climatology (Gouretski and Koltermann 2004) shows that the Atlantic is slightly too fresh and the Pacific slightly too salty. The too salty and slightly too warm anomaly south of Newfoundland is caused by the simulated path of the Gulf Stream, which separates from the coast too far north in the model. The Arctic is too fresh, typically by more than 1‰ with values of more than 2‰ off Siberia related to the too strong freshwater input into the Arctic. The salinity error near Bering Strait is smaller than in the other parts of the Arctic due to the inflow of relatively well reproduced North Pacific surface water. In the subtropical upwelling zones off California and South America, the simulated near-surface salinity is overestimated in comparison to climatology. This is caused by the compensation of the too strong solar heating by evaporative cooling.

The basic structures of the observed heat flux field are generally reproduced by the model (Fig. 7a, b). At the equator, the heat flux from the atmosphere to the ocean is positive. Maxima are reached in the eastern part of the basins. The modelled zone is broader than in the NCEP reanalysis data (Kalnay et al. 1996),

Fig. 6 Climatological distribution of modelled (a) and difference between modelled and observed (interpolated from the WGHC climatology) salinity at 75 m depth (b). Units are ‰

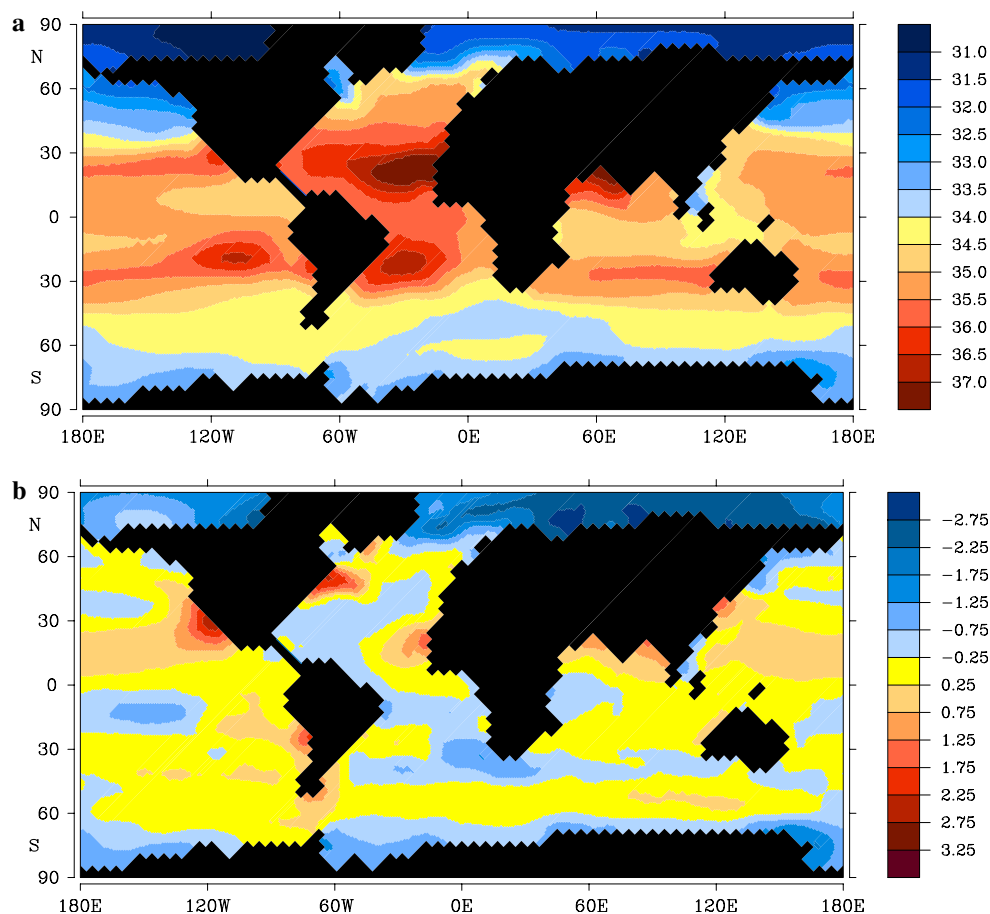
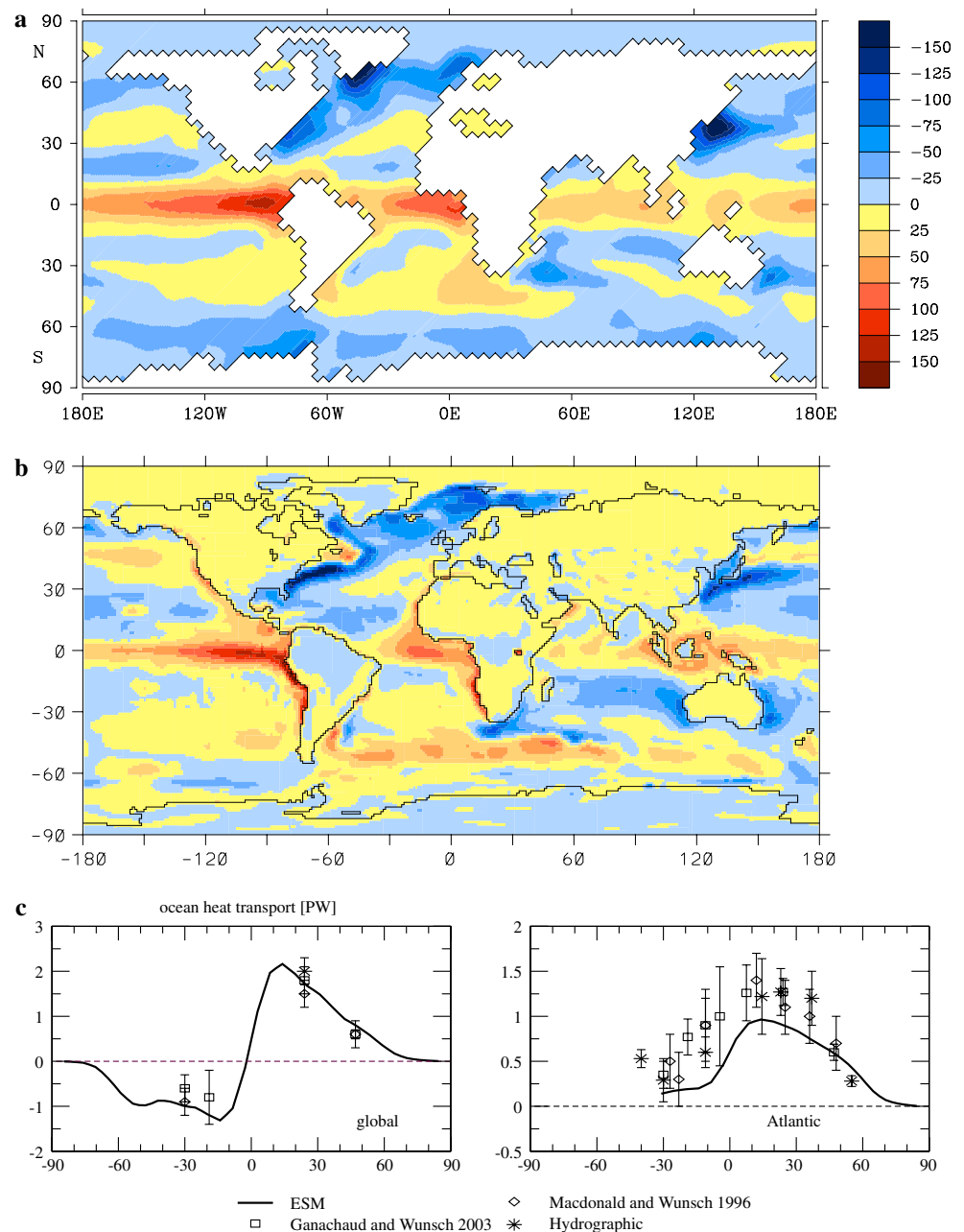


Fig. 7 **a** Modelled climatological air sea heat exchange. Negative values indicate heat loss of the ocean in W/m². **b** Mean net surface heat flux from the NCEP reanalysis (Kalnay et al. 1996). **c** Northward ocean heat transport for the global and Atlantic ocean in PW. Displayed are the model climate, results from inverse models (Macdonald and Wunsch 1996; Ganachaud and Wunsch 2003) and direct hydrographic observations (Atlantic: Bacon 1997 at 55°N; Lavin et al. 1998 at 24°N; Klein et al. 1995 at 14.5°S; Speer et al. 1996 at 11°S; Saunders and King 1995 at 40°S; Holfort and Siedler 2001 at 30°S. The global estimate is the sum of Bryden et al. 1991 for the North Pacific and Lavin et al. for the Atlantic)



which is a consequence of the coarse resolution of the model. In the Pacific peak values exceed 125 W/m²; in the Atlantic they are somewhat lower. The Pacific values are quite realistic; in the Atlantic, they are slightly too high. The model strongly underestimates the heat uptake in the subtropical upwelling zones near the eastern margins of Pacific and Atlantic. This results because the coastal upwelling has not been well resolved in the model. In the North Atlantic, the model reproduces the band of strong oceanic heat loss associated with the Gulf Stream and its extensions into the Nordic Seas. The heat uptake by the cold southward flowing Newfoundland current is not reproduced in the

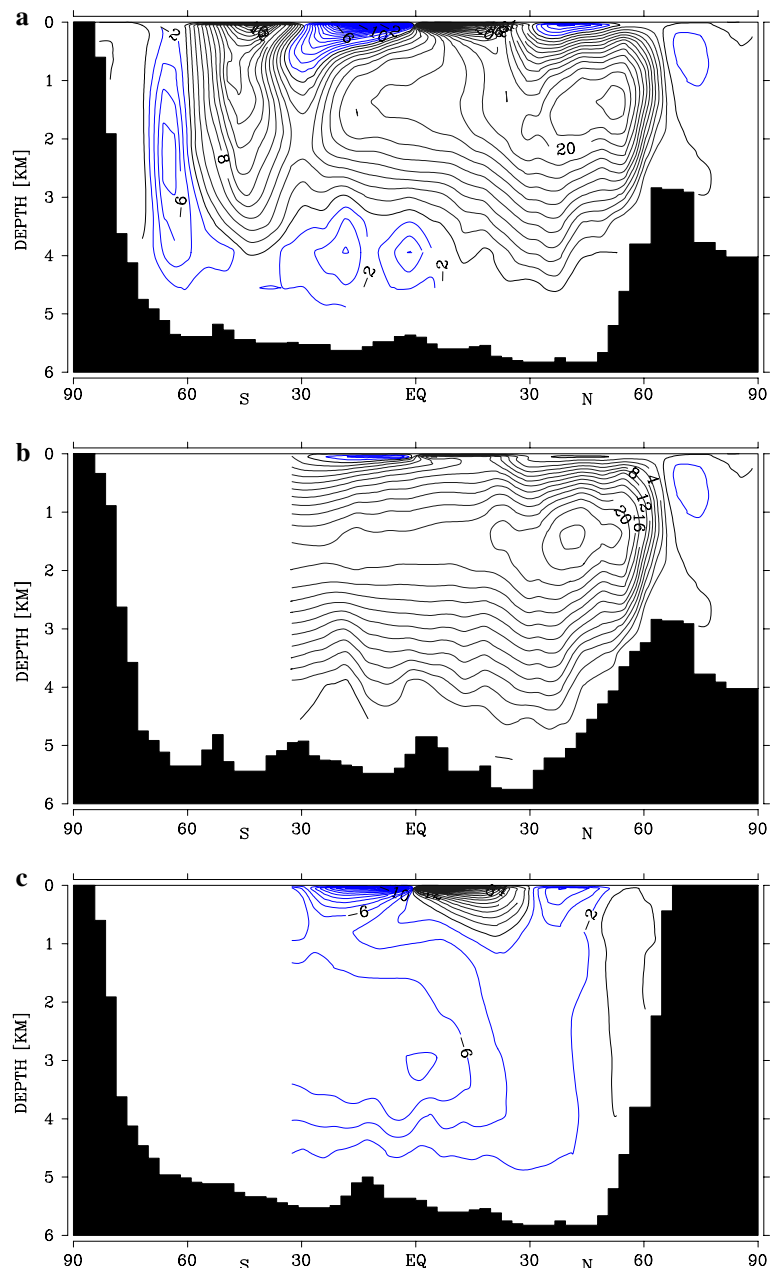
model. Close to Antarctica, the model simulates heat loss. The basic structure of the oceanic heat transport (Fig. 7c) is reproduced well in the model. The modelled northward heat transport of the Atlantic reaches almost 1 PW at 20°N, whereas the observational estimates scatter around 1.2 PW (e.g. Ganachaud and Wunsch 2003). At 48°N the model produces 0.57 PW ocean heat transport, compared to 0.65 ± 0.25 PW from Macdonald and Wunsch (1996) and 0.6 ± 0.09 PW by Ganachaud and Wunsch (2003). The Atlantic northward oceanic heat transports is at almost all latitudes lower than the observed values, but lies almost everywhere within the (quite large) error bars.

The global ocean heat transport of the model agrees well with the estimates.

The model shows a strong conveyor belt circulation in the Atlantic with a peak value of the North Atlantic deep water (NADW) overturning cell of 26 Sv and an outflow of 20 Sv to the Southern Ocean (Fig. 8). This cell is somewhat stronger than estimates from observations, which estimate the maximum overturning around 20 Sv and the strength of the outflow of NADW to the Southern Ocean between 15 and 20 Sv (e.g. Schmitz 1995; Ganachaud and Wunsch 2000; Talley et al. 2003). The strongest deviation from the

observed pattern is the absence of the Antarctic bottom water (AABW) cell. This is an effect of the long term mean presented here. At 30°S and 4 km depth, the simulated decadal mean Atlantic overturning stream function varies between an outflow of 3 Sv and an inflow of 2 Sv of AABW. These variations are connected to fluctuations in the formation rate of AABW. The characteristic time scale lies at 400 years. The underlying mechanism is the slow build up of warm and deep salty water around Antarctica in times of weak AABW formation. When this relatively warm water reaches the surface layers, it gets strongly cooled

Fig. 8 Overturning stream function for the global ocean (a), Atlantic (b) and Pacific (c). Units are Sverdrup. Positive values indicate a clockwise circulation



and initiates a period with strong AABW formation. The reason is most likely due to a relatively high amount of freshwater input from the atmosphere, which does not permit continuous AABW formation. The presence of these long-term variations is independent from being modelled in the fully synchronously or in the periodically-synchronously coupled mode.

The Northern Hemisphere ice sheets in the control run have an area of $2.15 \times 10^6 \text{ km}^2$. Beside the Greenland ice sheet, minor ice caps are simulated in Svalbard, Iceland, and Baffin Island. According to Church et al. (2001), the area of the Greenland ice sheet is 1.71 million km², and the volume is 7.2 m sea level equivalent (SLE). The simulated Northern Hemisphere ice sheets volume is 8.6 m SLE. The main deviations of the simulated ice sheets from the real ones are found in northwest Greenland, where the ice thickness is underestimated by several hundred meters and in northeast Greenland, where the simulated ice sheet extends onto the shelf areas. The central (in longitude) part of the ice sheet is lower by 100–200 m compared to observations.

The simulated Antarctic ice sheet area ($12.70 \times 10^6 \text{ km}^2$) exceeds the estimate of Church et al. (2001) by 3%. Its volume ($66.94 \times 10^6 \text{ km}^3$) is overestimated by 9%. All figures given here correspond only to grounded ice (i.e. the area and volume of the ice shelves have not been accounted for). The ice excess is placed in West Antarctica and the area of the Amery Ice Shelf. For further details of the control ice sheets, see Vizcaíno (2006).

3 Experiments

The model was forced with anthropogenic CO₂ emissions starting from the year 1751 (see Fig. 9). All other forcings were kept constant as in the control run. Up to year 2000, historic emissions were prescribed (Marland et al. 2005; Houghton and Hackler 2002). From the year 2001–2100, three different SRES emission scenarios have been used (Nakicenovic et al. 2001): the high emission scenario A2 peaking in emissions of 29.1 Pg C year⁻¹ in the year 2100, the intermediate emission scenario A1B with peak emissions of 16.4 Pg C year⁻¹ in 2050 and a gradual reduction to 13.5 Pg C year⁻¹ in 2100, and the low emission scenario B1 with peak emissions of 11.7 Pg C year⁻¹ in 2040 and a strong reduction to 4.2 Pg C year⁻¹ in the year 2100. As the scenarios were developed only up to 2100, we assumed a gradual reduction of the emissions after 2100 in all scenarios

using an exponential decay with a time constant of 150 years. Up to the year 3000 the scenarios result in total emissions of 1,969 (B1), 3,812 (A1B) and 6,568 Pg C (A2). During the next 1,000 years the emissions are very small and the total emissions increase only very little to 1,970, 3,817 and 6,579 Pg C. The historical emissions up to the year 2000 correspond to a total value of 439 Pg C, of which 156 Pg C originate from land use changes.

Analogously to previous studies (Friedlingstein et al. 2003), the following simplified assumptions were made for future emission scenarios: The land surface model does not include land use changes and calculates potential vegetation only (so changes in land use are represented in the emissions, but not in the vegetation distribution of the model). Anthropogenic nitrogen sources were neglected, and sulphate emissions were ignored. Moreover, the earth system model does not consider changes in dust, although future changes in the aerosol loading might be of importance for the coupling between climate and marine biosphere (Jickells et al. 2005).

3.1 Historical experiments 1751–2000

In order to discriminate between the signal and natural variability of the system, an ensemble simulation was carried out. The size of the ensemble simulations is five, with the individual simulations starting from years 0, 200, 400, 600, and 800 of the control run with prescribed anthropogenic CO₂ emissions of 1751.

The resulting atmospheric CO₂ concentration is shown in Fig. 10a. In general, the model reproduces the observed atmospheric CO₂ concentration quite well. The deviations between the model's global mean atmospheric CO₂ concentrations and the observed station measurements is, for most data points, less than 6.4 ppm, which corresponds to two standard deviations of the atmospheric CO₂ concentration calculated from the control run (Fig. 10b). The only markable exception is the period between 1880 and 1940, where two realisations underestimate the atmospheric CO₂ concentrations by up to 15 ppm.

The average CO₂ uptake for 1980–1989 is 2.2 Pg C year⁻¹ for the ocean and 2.1 Pg C year⁻¹ for the terrestrial biosphere. For 1990–1999, uptake is 2.2 Pg C year⁻¹ for the ocean and 2.7 Pg C year⁻¹ for the terrestrial biosphere. These values are in the upper range of the OCMIP estimates for the ocean (1.5–2.2 Pg C year⁻¹, Orr et al. 2001), and well within the range of the IPCC budgets from the special report on land use, land use change and forestry (ocean 2.0 ± 0.8 and terrestrial biosphere 1.9 ± 1.3 for 1980–1989, ocean

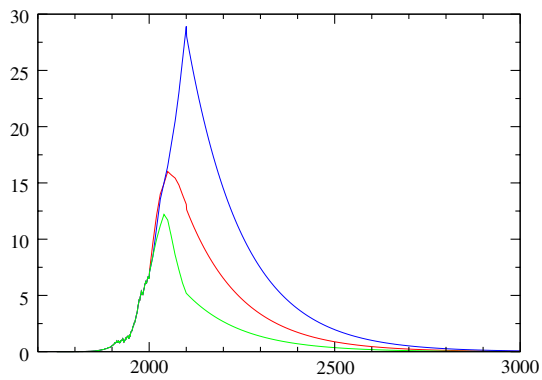


Fig. 9 Time series of prescribed CO₂ emissions. Units are Pg C year⁻¹. Up to the year 2000, historical emissions are used; between 2001 and 2100, the emissions follow SRES scenarios A2 (blue), A1B (red), and B1 (green). From 2101 onward, an exponential decay with a time constant of 150 years is assumed

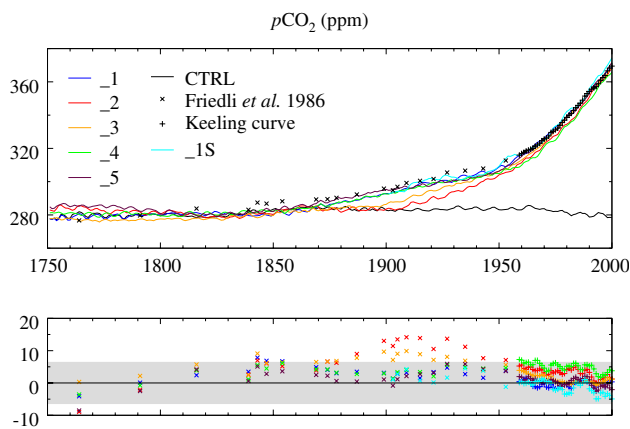


Fig. 10 *Top* Time series of modelled and observed atmospheric CO₂ concentration, in ppm. Model experiment “_1” starts in year 0 of the control run, “_2” in year 200, etc. *Bottom* Deviations between observed and modelled atmospheric CO₂ concentration. The grey bar indicates two times the standard deviation from the control run

2.3 ± 0.8 and terrestrial biosphere 2.3 ± 1.3 for 1989–1998, Watson et al. 2000).

In the year 2000, the simulated increase in terrestrial carbon (relative to 1750) is 114 Pg C (using the mean of the control run as reference). The net release of the terrestrial biosphere (taking into account the prescribed emissions from land use change) is 42 Pg C. The spread of this value is quite large between different members of the ensemble, extreme values of 32 and 56 Pg C occur.

In the year 2000, the model has simulated a warming of 0.2 K in the global mean SST fields. The net oceanic heat uptake for the five ensemble members lies between 0.07 and 0.18 PW. The response in global mean

near surface air temperature varies in the different realisations between 0.15 and 0.57 K, with most realisations between 0.3 and 0.45 K. The latest IPCC report (Houghton et al. 2001) gives an estimate of the warming of the global mean near-surface air temperature of 0.6 K since the end of the 19th century. However, the ESM does not include other anthropogenic greenhouse gases than CO₂, and the effect of aerosols is not included, either. Both effects are likely to have influenced the observed climate change. The periodically synchronous coupling technique could have introduced an artificial delay in the simulated response.

3.2 Future changes

The integrations were continued with forcing from SRES CO₂ emission scenarios A2, A1B, and B1 (Nakicenovic et al. 2001). Three ensemble runs were carried out for scenarios A2 and B1, five for scenario A1B. All simulations were integrated until the year 3000, and for each scenario at least one simulation was prolonged until the year 5000 in order to achieve a better estimate of the equilibration process of the system. A list of the experiments is given in Table 1. The effect of changing climate on the carbon cycle is investigated in additional experiments, where the radiative forcing in the atmosphere was calculated with an atmospheric CO₂ concentration of 280 ppm (B1-280, A1B-280, A2-280). In one simulation (A2-NO-ICE), the ice sheets are prescribed in order to estimate the effect of ice sheets on future climate changes.

3.2.1 2001–2100

For 2100, the scenarios result in CO₂ concentrations of 506 ppm (B1), 656 ppm (A1B), and 778 ppm (A2) (805 ppm for the synchronous A2 experiment). Similar studies with the A2 scenario reach 770 ppm (Dufresne et al. 2002; Friedlingstein et al. 2003) and 732 ppm (Govindasamy et al. 2005) for this time. The IPCC (Houghton et al. 2001) provides estimates from two different models, modelled atmospheric CO₂ concentrations for 2100 are 549 ppm (B1), 717 ppm (A1B), and 856 ppm (A2) for the ISAM model, and 540 ppm (B1), 703 ppm (A1B), and 836 ppm (A2) for the Bern-CC model. Our estimates of the atmospheric CO₂ concentration are generally lower than the IPCC results, but our A2 estimate agrees quite well with the results by Friedlingstein et al. (2003) and Govindasamy et al. (2005). Uncertainties in the predicted CO₂ concentration due to natural variability of the system can be estimated from the standard deviations between the

Table 1 List of experiments

Name	Length	Forcing	Integration mode
CTRL	2,250	–	8/2 fixed until 1000 1001–2250 48/2 with cut off criterion
CTRLS	1,000	–	Fully synchronous
A2_*	1,751–3,000/5,000	SRES A2	8/2 fixed until 3000 From 3001: 48/2 with cut off criterion
A1B_*	1,751–3,000/5,000	SRES A1B	8/2 fixed until 3000 From 3001: 48/2 with cut off criterion
B1_*	1,751–3,000/5,000	SRES B1	8/2 fixed until 1250 From 3001: 48/2 with cut off criterion
A2_1S	1,901–2,500	SRES A2	Fully synchronous
A2-NOICE	1,751–5,000	SRES A2	As A2_1, but ice sheets prescribed
A2-280	1,751–4,000	SRES A2	As A2_1, variable cut off criterion for entire experiment, atmospheric radiation calculated with atmospheric CO ₂ concentration of 280 ppm
A1B-280	1,751–3,000	SRES A1B	As A1B_1, variable cut off criterion for entire experiment, atmospheric radiation calculated with atmospheric CO ₂ concentration of 280 ppm
B1-280	1,751–3,000	SRES B1	As B1_1, variable cut off criterion for entire experiment, atmospheric radiation calculated with atmospheric CO ₂ concentration of 280 ppm

Experiments with names ending with “_1” start in year 0 of the CTRL experiment, “_2” in year 200, “_3” in year 400, etc. A1B-on refers to experiments A1B_2 and A1B_5, A1B-off to experiments A1B_1 and A1B_3

ensembles, they are 2.8 ppm (B1), 11.2 ppm (A1B), and 5.0 ppm (A2), averaged for the period between 2001 and 3000, compared to a standard deviation of 3.2 ppm for the control run. In the year 2100, the simulated atmospheric CO₂ concentrations in the experiments without climate change are between 40 (A2-280 and A1B-280) and 20 ppm (B1-280) lower than in the corresponding experiments with climate change. The increase in carbon content for the year 2100 (compared to the preindustrial control run) is 567 Pg C for the terrestrial biosphere and 596 Pg C for the ocean of the A2 scenario. Although our A2 experiments and the studies mentioned before agree quite well on the atmospheric increase, the distribution of carbon over terrestrial biosphere and ocean highly differs: Dufresne et al. (2002) and Friedlingstein et al. (2003) estimate 480 and 700 Pg C, and Govindasamy et al. (2005) estimate 919 and 350 Pg C, for terrestrial biosphere and ocean respectively. These differences can be caused by differences in the models used for the terrestrial and marine carbon storage, as well as by differences in the predicted climate. The differences in the terrestrial carbon storage in the experiments by Govindasamy et al. (2005) and our experiments are large. Both the LPJ model (Sitch et al. 2003) and the IBIS vegetation model (Foley et al. 1996), as used by Govindasamy et al. (2005), are known to react strongly to CO₂ fertilisation. However, the heterotrophic respiration in the LPJ model reacts much more to temperature changes than the IBIS model (Cramer

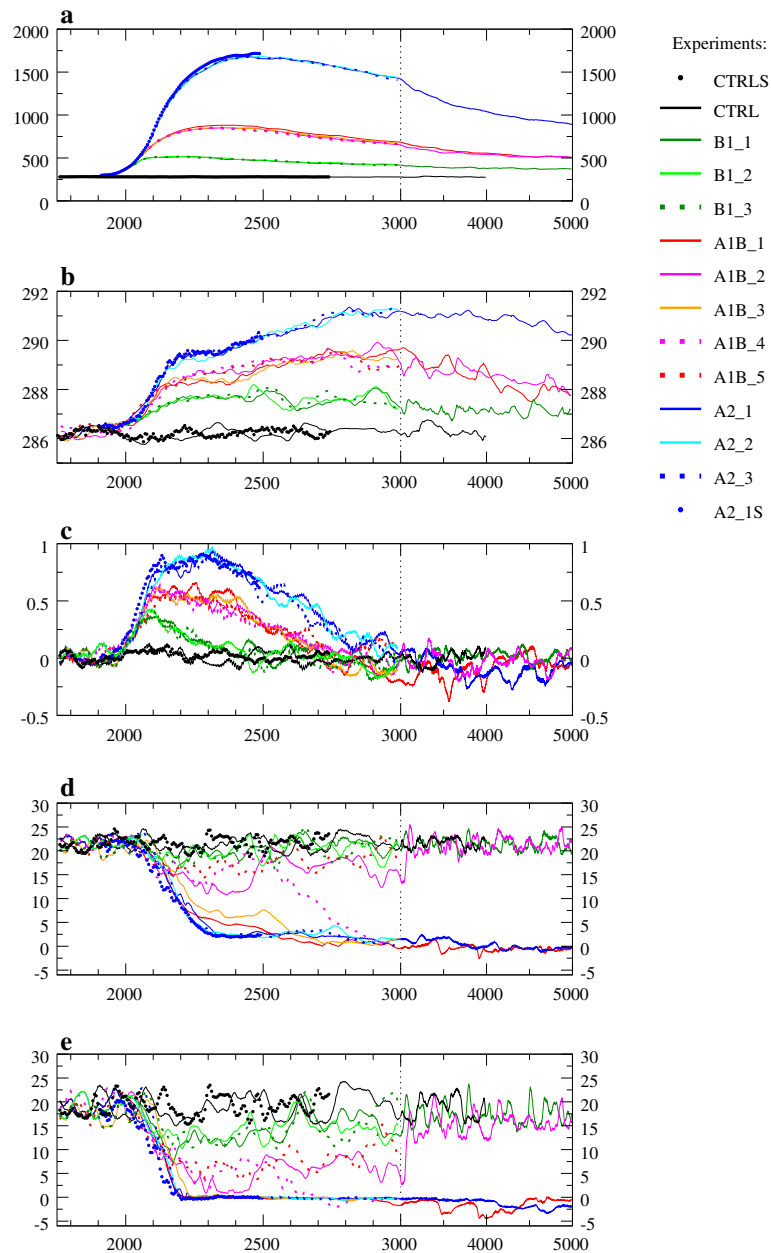
et al. 2001), which causes the combined effect (CO₂ and climate change) to be stronger in the IBIS model. The difference in temperature sensitivity of the climate model could play a major role: whereas Dufresne et al. (2002) show a global temperature increase of 3 K and Govindasamy et al. (2005) show an increase of 3.2 K, our experiments show an increase of only 1.6 K (Fig. 11b) for the year 2100 compared to the pre-industrial climate. This causes in our simulation the (positive) CO₂ fertilisation effect to be relatively important compared to the (negative) effect of enhanced respiration due to higher temperatures.

3.2.2 Atmospheric CO₂ concentration

The peak concentrations reached in these scenarios are approximately 1,680 ppm (A2 near the year 2500), 855 ppm (A1B near the year 2330), and 520 ppm (B1 near the year 2200). In the simulations without climate change, the peak concentrations are 1,249 (A2 near the year 2380), 718 (A1B-280 near the year 2290), and 485 ppm (B1-280 near the year 2100). Thus climate change reduces the ability of ocean and land vegetation/soil to take up anthropogenic carbon quite considerably. The climate effect increases with higher CO₂ concentrations. In the A2 scenario, the peak in increase in atmospheric carbon content is 30% lower if climate changes are neglected.

The atmospheric CO₂ concentrations in the year 3000 end with 1,416 (A2), 665 (A1B), and 416 ppm

Fig. 11 Time series of simulated integral model quantities. **a** Atmospheric CO₂ concentration in ppm. **b** Global mean near surface air temperature in K. **c** Globally integrated oceanic heat uptake in PW. **d** Strength of the North Atlantic overturning stream function at 30°N at 1,500 m depth in Sv. **e** As **(d)** but at 2,500 m depth. All plots show 20-year running mean values. For the description of the experiments, see Table 1. Note the non-constant scale of the *x*-axis!



(B1). In the experiments without climate change, the corresponding values are 969 (A2-280), 556 (A1B-280), and 396 ppm (B1-280). Our results confirm previous studies about the importance of the climate feedback on uptake of anthropogenic carbon (e.g. Friedlingstein et al. 2003; Fung et al. 2005; Winguth et al. 2005).

3.2.3 Atmosphere and ocean climate

Averaged over the period 2801–3000, the simulated global mean near surface air temperature has increased by 4.9 (A2), 3.0 (A1B), and 1.3 K (B1) for the three scenarios (relative to the climate of the control run without anthropogenic forcing, see Fig. 11b). Using

these values to estimate the equilibrium climate sensitivity of the coupled model, this yields a mean estimate of 2.3 K for CO₂ doubling. An exact estimate would require a simulation with a perfect equilibrium, which is not the case here, but the error is likely to be small. This value is at the lower end of climate sensitivities estimated from near-equilibrium runs from the latest IPCC report (Houghton et al. 2001), where a mean sensitivity of 3.5 K is given.

Between the years 3000 and 5000 the global temperatures are very slowly decreasing. The trends are typically around -0.4 K/1,000 years for the A1B and A2 experiments, whereas the trend in the B1_1 experiment is not substantially different from the

simulated long-term trends of the control run. These weak temperature changes are caused by the counterbalancing effects of the long-term response of surface air temperature to the early CO₂ increase and the slightly stronger response to the slowly sinking atmospheric CO₂ concentrations related to the oceanic uptake of anthropogenic carbon.

The global mean ocean heat uptake (see Fig. 11c) in scenario A1B shows maximum values of 0.6 PW between the years 2100 and 2200, and decreases strongly from the year 2400 onwards. In the A2 experiments, maximum ocean heat uptake reaches approximately 0.9 PW in the year 2200. In the very moderate scenario B1, the maximum ocean heat uptake does not exceed 0.4 PW close to the year 2100. In the year 3000 the net ocean heat uptake in all experiments has decreased so much that it lies almost within the range of variability of the control run.

The changes in the meridional overturning circulation of the North Atlantic (NAMOC, see Fig. 11d, e) reveal a strong sensitivity on the scenario. In the low emission scenario B1, the NAMOC is almost unchanged during the entire experiment (maximum reduction approximately 2–3 Sv). In the high emission scenario A2 and in scenario A1B, the NAMOC in year 2100 is reduced to values between 16 and 21 Sv, compared to 21.5 Sv in the long-term mean of the control run. The simulated weakening of between 0 and 25% in the individual ensemble members lies in the lower half of the range for corresponding scenario A1B simulations performed with various models. Schmittner et al. (2005) report a mean weakening by 25% with an error bar of 25% for these simulations. In all A2 simulations, however, the deep water formation in the North Atlantic collapses completely in the year 2250, and in year 3000 the NADW cell has vanished. The extended simulation until the year 5000 shows no indications of a recovery. The experiments forced with SRES emission scenario A1B behave similar to the A2 experiments until the year 2100. In the following years, however, the individual ensemble members behave quite differently. The model response ranges from experiments with a relatively fast collapse to experiments with a temporary, moderate reduction of the NAMOC. Here, the model is obviously close to a bifurcation point, the threshold for the NAMOC seems to be close to 10 Sv. Whereas two experiments make the transition during the strong warming phase between the years 2150 and 2250, one experiment crosses the threshold between the years 2600 and 2750, a period where the rate of change of surface temperatures is already rather small. The weakening of the NAMOC is always associated with a

much shallower NAMOC, indicated by the much stronger reduction at 2,500 m than at 1,500 m. Whereas the NAMOC at 1,500 m in the A1B_2 simulation has almost the same strength after the year 3000 as the control run, the NAMOC at 2,500 m (see Fig. 11e) shows substantially reduced values. The reduction and collapse of the deep convection in the North Atlantic delays the global mean warming. This is visible as a relative plateau in the time series of, e.g. the A2 experiments between the years 2200 and 2350 (Fig. 11b).

In their atmosphere–ocean model, Manabe and Stouffer (1994) report a collapse of the NAMOC of several millennia duration for a $4 \times \text{CO}_2$ experiment, whereas a corresponding $2 \times \text{CO}_2$ experiment showed only a temporary reduction with slow recovery. In corresponding experiments, Voss and Mikolajewicz (2001a) achieved, in both cases, only a reduction with slow partial recovery. The collapsed A2 simulations correspond roughly to $5 \times \text{CO}_2$ experiments, whereas the atmospheric CO₂ concentration in the non-collapsing B1 experiments always stays below the $2 \times \text{CO}_2$ level. Mode transitions in the A1B experiments occur between the $2 \times$ and $3 \times \text{CO}_2$ levels, but the A1B-on simulations experience, for some time, atmospheric concentrations slightly higher than three times the preindustrial control value of 280 ppm. Winguth et al. (2005) report a collapse of the NAMOC for a $4 \times \text{CO}_2$ experiment with the present ESM, whereas the $2 \times \text{CO}_2$ and $3 \times \text{CO}_2$ experiments resulted in a weaker, but non-collapsed NAMOC.

For the near surface air temperature, the B1 simulations show a distinct warming pattern (see Fig. 12a). Over the ocean, the warming is roughly 1 K; over most of the land, the warming is between 1 and 2 K. Exceptions are the desert areas of North Africa and Southwest Asia and the high northern latitudes with a warming between 2 and 3 K. In the northwest Pacific and close to the deep water formation sites of the Southern Ocean, strong warming is simulated due to reduced sea ice coverage. In the southern Indian Ocean, the southeast Pacific, and directly at the southeast coast of Greenland, areas of slight warming or even cooling are simulated. In the North Atlantic, these are the consequences of reduced deep convection. This pattern shows large similarities with the warming pattern shown in the IPCC report (Fig. 9, 10 in Houghton et al. 2001) for the end of this century. Exceptions are the areas in the northern Atlantic and the Southern Ocean, where our simulation is much closer to equilibrium and thus warmer.

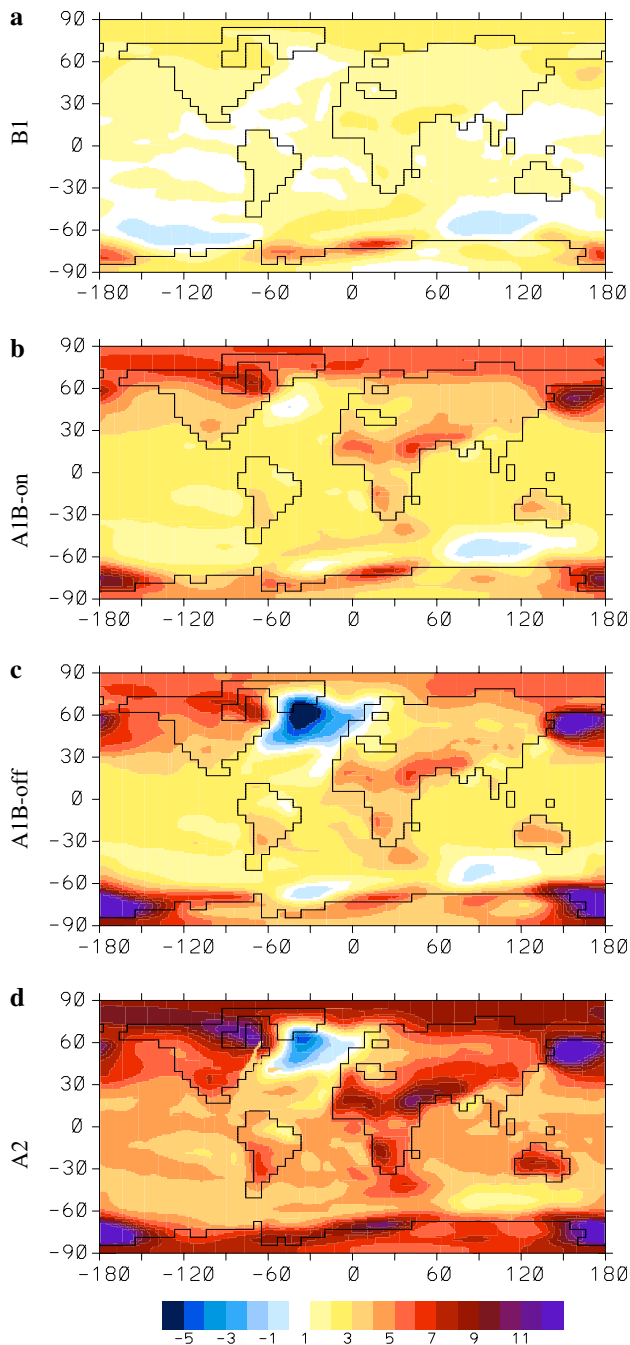


Fig. 12 Annual mean change in near surface air temperature for B1 (a), A1B-on (b), A1B-off (c), and A2 simulations (d). Displayed are ensemble averages over the years 2801–3000. Units are K. Reference value is the climate of the control run

For scenario A1B temperature anomalies are shown in Fig. 12b and c. The average of experiments A1B_2 and A1B_5 (henceforth also called A1B-on), which both have a non-collapsed NADW cell, shows essentially the same spatial pattern as in the B1 experiments, but with stronger amplitude. The typical ocean warming lies between 2 and 3 K, and the land between 3 and

4 K. Sahara and high northern latitudes show, in many places, more than 5 K warming. Over the ocean, maximum warming occurs in the Ross and Weddell Sea and in the northwest Pacific associated with a strong reduction in sea ice cover.

The change in near surface air temperature in the two simulations A1B_1 and A1B_3 (henceforth referred to as A1B-off) with a fast collapse of the NADW cell is shown in Fig. 12c. The strong cooling southeast of Greenland is absent in the A1B-on simulations. Strong warming is simulated in the northwest Pacific (more than 8 K) and in the Ross Sea (>12 K). These two regions are associated with enhanced convection. In the North Pacific, a strong, relatively shallow overturning cell has developed with enhanced pole ward oceanic heat transport (see below).

In the high emission A2 scenario, the NADW cell collapses in all simulations. The surface warming pattern (Fig. 12d) is very similar to the previously described pattern of the A1B-off simulations. The Arctic shows a mean warming of 8–9 K. Peak warming of more than 11 K is simulated in Somalia, northeast Canada, over the northwest Pacific, and in the Ross Sea. The dry land areas in the subtropics show warming signals of typically more than 7 K. Close to the southeast coast of Greenland, a cooling of 5 K is simulated. In contrast to the collapsed A1B simulations, Europe shows a warming everywhere due to the higher CO₂ concentration, but the warming over northwest Europe is relatively small. The warming over the oceans lies typically between 3 and 5 K.

The hydrological cycle is enhanced in all greenhouse experiments. Averaged over the years 2801–3000, the total amount of precipitation is increased by 3, 7 and 12% for scenarios B1, A1B, and A2, respectively. On average, the hydrological cycle increases by 5.1% for CO₂ doubling, compared to 6.6% given in the IPCC 2001 report (Houghton et al. 2001). The rate of enhancement in relation to the warming varies between the experiments and increases with increasing warming: 2.0%/K in scenario B1 and 2.4% /K in scenario A2. These values are consistent with the values found by Voss and Mikolajewicz (2001a) for the ECHAM3.2/LSG1 model. For this parameter, our model shows a relatively high response compared to other models.

The change in atmospheric moisture transports between A1B_2 (an experiment with non-collapsed NAMOC) and the control run is displayed in Fig. 13, together with the climate of the control run. To first order the changes in moisture transport in this simulation reflect just an enhancement of the transport pattern of the control run. Exceptions are the subtropics and the Indian Ocean. The pole ward atmo-

spheric moisture transport is enhanced in all oceans. As a consequence, the Arctic and the Atlantic north of 60°N receive 0.1 Sv more freshwater from atmosphere, rivers, and Greenland; the Southern Ocean (south of 45°S) receives almost 0.2 Sv more freshwater. The atmospheric moisture transport across North America increases by 50%, adding 0.16 Sv additional freshwater input to the Atlantic (see Table 2; Fig. 14^{top}). In the tropics, however, the Atlantic export across America towards the Pacific is strongly enhanced. Together with an additional net export across Africa, Asia, and by transports towards the Southern Ocean, this almost completely cancels out the increased import across North America. The Atlantic north of 30°N and the Arctic receive together almost 0.1 Sv more freshwater input from anomalous convergence of atmospheric moisture transports (see Fig. 14^{top}). These changes in interbasin moisture transports explain the weakening of the NADW formation in the North Atlantic seen in almost all experiments.

In the North Pacific, the anomalous atmospheric moisture transports are divergent, associated with anomalous net evaporation in this region. As a consequence of these changes in atmospheric moisture transport, the northwest Atlantic becomes fresher (between 0.25 and more than 0.5‰) and the North Pacific becomes saltier (more than 0.5‰ in the northwest Pacific, regionally more than 1‰) (not shown). The saltier surface waters reduce the vertical stability in the northwest Pacific quite substantially.

In the experiments with collapsed NADW cell (A1B-off), the convection in the northwest Pacific gradually deepens and induces a shallow meridional overturning cell. The associated ocean heat transport leads to an additional surface warming in the northwest Pacific (see Fig. 12), further enhancing evaporation. In the North Atlantic, the colder surface temperatures reduce evaporation. The resulting anomaly between a simulation with convection in the North Pacific and a simulation with convection in the North Atlantic is

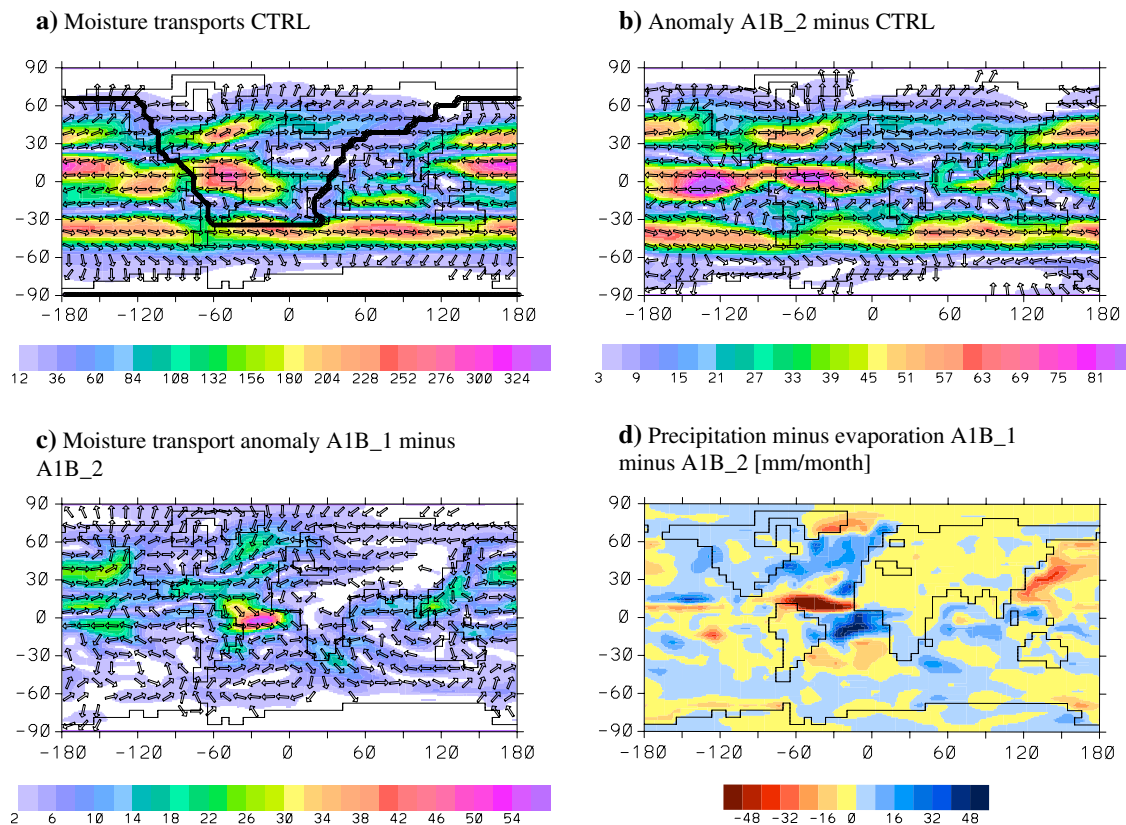


Fig. 13 Vertically integrated atmospheric moisture transports in $\text{kg m}^{-1} \text{s}^{-1}$. **a** Climate of the control run. The crosses indicate the watersheds used for the calculation of interbasin transports in Table 2. **b** Difference between A1B₂ (mean over the years 2801–3000) and control run. **c** Difference between A1B₁ and

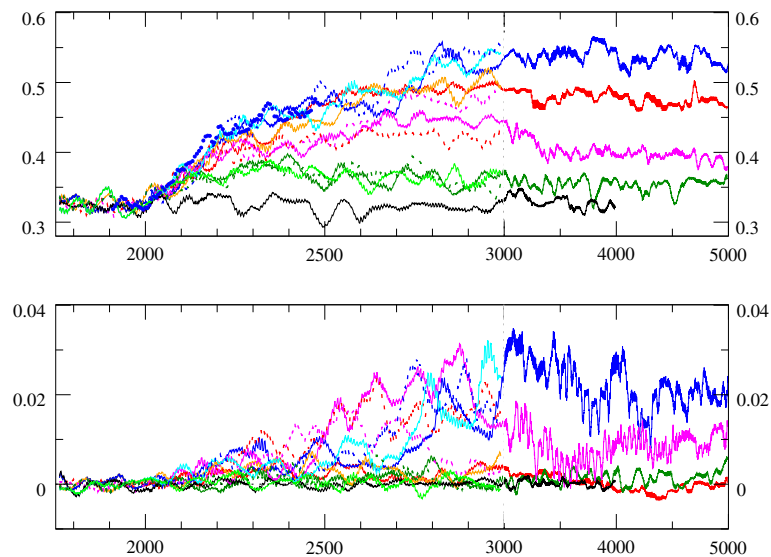
A1B₂ (mean over the years 2801–3000). **d** Difference in precipitation minus evaporation between A1B₁ and A1B₂ (mean over the years 2801–3000) in mm/month. Only every second vector in each direction is shown

Table 2 Vertically integrated atmospheric moisture transports into the Atlantic catchment area north of 30°S

Arctic and Atlantic to 30°S (mSv)	CTRL	A1B_2-CTRL	A1B_1-A1B_2
North America	329	164	61
South America	-331	-68	-17
Atlantic across 30°S	-363	-35	5
Africa	96	-25	-9
Asia	-87	-36	12
Total input north of 30°S	-355	-1	52
Total input north of 30°N	256	68	70

Data are averaged over the years 2801–3000. The watersheds are indicated in Fig. 13a. Units are 1,000 m³/s

Fig. 14 Time series of net freshwater input in the North Atlantic (north of 30°N) and the Arctic (*top*) and the melt water input from northern hemisphere glaciers (*bottom*). Displayed are running averages over 20 years. The unit for both panels are Sv. For the colours of the individual experiments, see Fig. 11. Note the non-constant scale of the *x*-axis!



shown in Fig. 13c and d. In the tropical Atlantic, the ITCZ is shifted towards the southeast. This pattern is quite similar to the shift of the ITCZ in experiments with a collapsed NAMOC in atmosphere-ocean GCMs (e.g. Manabe and Stouffer 1988; Schiller et al. 1997). An additional moisture export from the North Pacific into the Arctic and across North America into the Atlantic is obvious. The main moisture source of the anomalous atmospheric moisture transport is in the northwest Pacific, the main sink in the northwest Atlantic. In total this export amounts to approximately 0.07 Sv. This is a strong feedback destabilising the present mode of ocean overturning circulation and explains why the NAMOC remains collapsed in some of the experiments.

In the more extreme scenario A2, changes in atmospheric moisture transport are so strong (see Fig. 14*top*) that all three ensemble members ended up in the mode without NADW formation and a completely stagnating deep Atlantic (see Fig. 11d, e). Towards the end of the A2 experiments, the total additional freshwater input into the North Atlantic (north of 30°N) and the Arctic amounts to more than 0.2 Sv (see Fig. 14*top*). In experiment A2_1 the ventilation of the deep Atlantic from the south with AABW

starts around the year 3500. The magnitude of the melt water input from the northern hemisphere ice sheets (basically Greenland) is an order of magnitude smaller than the input from changes in atmospheric moisture transports (compare panels of Fig. 14). Peak values of 0.03 Sv are reached in exp. A2_1 around the year 3000. Before the year 2500, when all but one collapses of the NAMOC occur, the melt water input does not exceed 0.01 Sv. The experiment without interactive ice sheets (A2-NOICE) shows basically the same behaviour as the other A2 simulations. In a series of stabilisation experiments at different CO₂ levels with the present model Winguth et al. (2005) did not see a difference in the behaviour of the NAMOC in the experiments with and without interactive ice sheets. Thus, the effect of melt water input from Greenland has only minor importance for the NAMOC in our simulations. However, in the A1B simulations the melt water input might have been important, as in the proximity of a bifurcation point small causes can lead to large effects. Stouffer et al. (2006) obtained a mean weakening of the NAMOC of 30% with a melt water input of 0.1 Sv in a recent model intercomparison study.

Jungclauss et al. (2006) or Swingedouw et al. (2006) found a moderate reduction of the simulated NAMOC

in case of an imposed/simulated melting rate of the Greenland ice sheet of about 0.1 Sv, which is much larger than the ice sheet melting simulated here.

Previous studies with GCMs gave quite different estimates of the relative importance of changes in atmospheric moisture transports in relation to the warming effect for the weakening of the NAMOC. Whereas Mikolajewicz and Voss (2000) have shown in the ECHAM3/LSG1 model that the surface warming contributes more to the weakening of the NAMOC than the enhanced freshwater supply into the North Atlantic, Dixon et al. (1999) arrived at the opposite result for their model. Gregory et al. (2005) showed in a model comparison that in most models the heat flux effect on the NAMOC is stronger than the freshwater effect. Latif et al. (2000) showed that their model did not show any weakening of the NAMOC due to strong moisture export from the tropical Atlantic to the tropical Pacific leading to increasing upper ocean salinity in the entire North Atlantic.

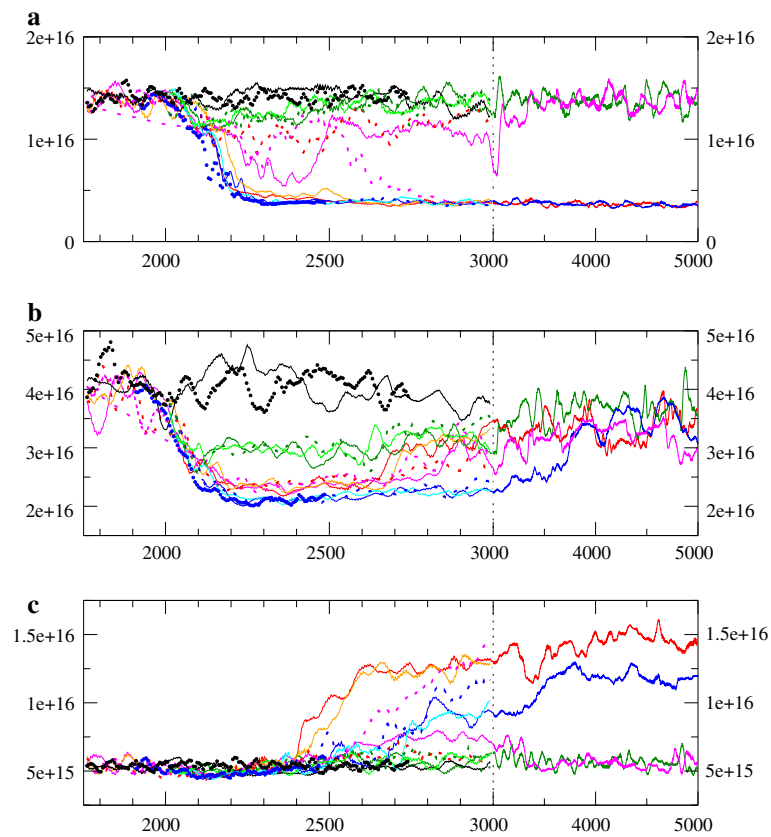
For each year and each experiment, the maximum depth of convection has been determined in order to elucidate the ventilation changes in the ocean (see Fig. 15). Integrated over the area of the ocean this yields an estimate of the amount of water which is in contact with the surface mixed layer each year. The absolute minimum value of this quantity is the thickness of the surface layer (50 m) multiplied with the area of the respective ocean basin. In the North Atlantic, the time series reflect the same changes as the time series of the overturning in the North Atlantic (Fig. 11d). Changes up to the year 2100 are moderate to small. Around the year 2200, the A2 experiments show a reduction to 30% of the unperturbed value within one century. In the collapsing A1B experiments, this transition appears as well, although somewhat delayed. All A1B experiments show a shallowing of convection around the years 2200–2250 with at least a temporal halving of the ventilated volume. The A1B-on simulations show some recovery to intermediate levels of deep convection, which is consistent with the shallowing of the NADW cell in these experiments. Interestingly, a sudden and strong reduction to less than 50% of the unperturbed value occurs in experiment A1B_2 between the years 3000 and 3100. Thereafter, this experiment recovers and reaches the same levels of ventilation as the B1 experiment around the year 3300. The signal in the B1 experiments is quite small with the strongest reduction by approximately 20% between the years 2100 and 2400.

In the Southern Ocean, all climate change experiments predict a weakening of the formation of AABW

(see Fig. 15b), with a strong reduction starting in the 21st century reaching minimal values between the years 2200 and 2300. This behaviour can be explained by the surface warming and the strongly enhanced atmospheric freshwater input south of 45°S (0.2 Sv in the A1B experiments). Minimal values of ventilated volume in the B1 experiment are typically around 75% and in the A1B and A2 experiments around 50% of the control run values. The recovery is relatively slow. Even in the year 5000, the ventilated volume is smaller than in the control run. It should be noted that the process of deep water formation on shelves is not very well simulated in this model, as the shelves are not well resolved. Thus the model forms most of its AABW by open ocean convection.

In the North Pacific, the behaviour is more complex (see Fig. 15c). Due to the surface warming, there is initially a slight reduction of the ventilated volume in all CO₂ experiments. But as the model has no deep convection in the North Pacific, this reduction is smaller than in the North Atlantic. Due to a poleward shift of the west wind belt in the North Pacific, the Kuroshio extends further northward (not shown). After the collapse of NADW formation in the A2 experiments the temperatures in the North Atlantic cool down substantially. This relative cooling extends—similar to other climate simulations with collapsed NAMOC (e.g. Schiller et al. 1997; Manabe and Stouffer 1997)—over the entire Northern Hemisphere. In winter, cold air outbreaks from Siberia together with reduced freshwater input reinforce the convection in the northwest Pacific. The effect is similar in the A1B-off experiments, but the delay between collapse in the North Atlantic and onset of convection in the North Pacific is shorter due to the weaker global mean warming. The area with convection deeper than 800 m, originally situated in the centre of the North Pacific, spreads westward until it reaches the coast. Around the year 2500, the associated shallow overturning cell develops rapidly. At this time, the formation of deep water both in the North Atlantic and in the Southern Ocean has been suppressed for more than 300 years, resulting in a stagnant deep Pacific. Due to the amplified freshwater fluxes, the meridional surface salinity gradient has been enhanced in the North Pacific. The shallow overturning cell advects this saltier subtropical water masses northward into the convection region, further enhancing the density of the water in the convective cell and further amplifying the overturning cell which gradually deepens to 2 km. The associated heat transport into the northwest Pacific increases surface temperatures and enhances evaporation, while the

Fig. 15 Time evolution of the ventilated volume in m³ for North Atlantic (a), Southern Ocean (b), and North Pacific (c). For the colours of the individual experiments, see Fig. 11. Note the non-constant scale of the x-axis!



precipitation is largely unchanged. In the North Atlantic, the effect is opposite. The onset of convection in the North Pacific and the collapse of North Atlantic convection is stabilised by the anomalous atmospheric moisture transports shown above for two different A1B experiments, with a strong anomalous moisture transport from the Pacific towards the Atlantic.

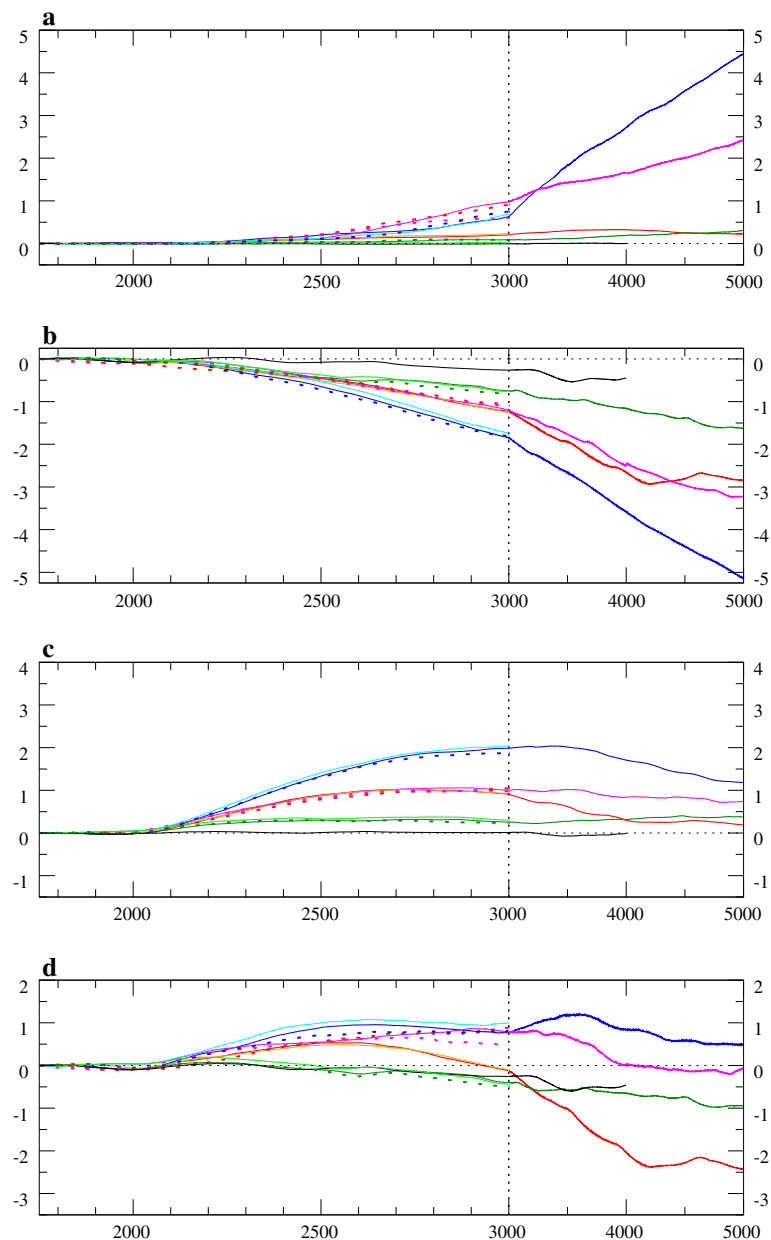
At the end of the experiment A1B_1, the North Pacific overturning cell reaches a strength of 18 Sv and extends down to 2,500 m depth. The deep inflow of AABW has a strength of 8 Sv. The deep Atlantic is ventilated entirely from the south (6 Sv AABW). The circulation pattern at the end of the A2_1 experiment is similar, but the ventilation of the deep Atlantic is still rather weak (2 Sv). A general enhancement of the formation of intermediate water in the North Pacific in case of a collapsed NAMOC cell has been found in other atmosphere–ocean models before (e.g. in an earth system model of intermediate complexity: Wright and Stocker 1993 or in an atmosphere–ocean GCM: Mikolajewicz et al. 1997). Saenko et al. (2004) demonstrate the possibility of strong deep water formation in the North Pacific in response to an imposed negative freshwater flux perturbation in the North Pacific.

3.2.4 Ice sheets and sea level

The evolution of the Greenland ice sheet is displayed in Fig. 16a. Until the year 2200, the changes are rather small. In the A1B-on experiments, a considerably reduced volume of the Greenland ice sheet is simulated for the year 3000. This change corresponds to approximately 0.9 m of global mean sea level. In the A1B-off simulations, this reduction in Greenland ice sheet volume is considerably smaller with approx. 0.2 m sea level equivalent (SLE). In the A2 experiments, the volume is reduced by 0.6 m SLE. In the following 1,000 years, the melting of Greenland is quite substantial, reducing the volume of the Greenland ice sheet to approximately two-thirds of its original value. In the A1B-on experiments the volume is reduced by 1.7 m SLE; in the A1B-off experiments by only 0.3 m SLE. In the B1 experiments, the change in volume of the Greenland ice sheet is rather small, with a reduction of 0.2 m SLE in the year 4000.

The distribution of changes in ice thickness is shown in Fig. 17. At the end of this millennium, a strong reduction in ice thickness near the coasts is simulated in the A1B-on experiments. This is caused by enhanced melting. The thickness in the interior of northern Greenland is increased due to enhanced accumulation.

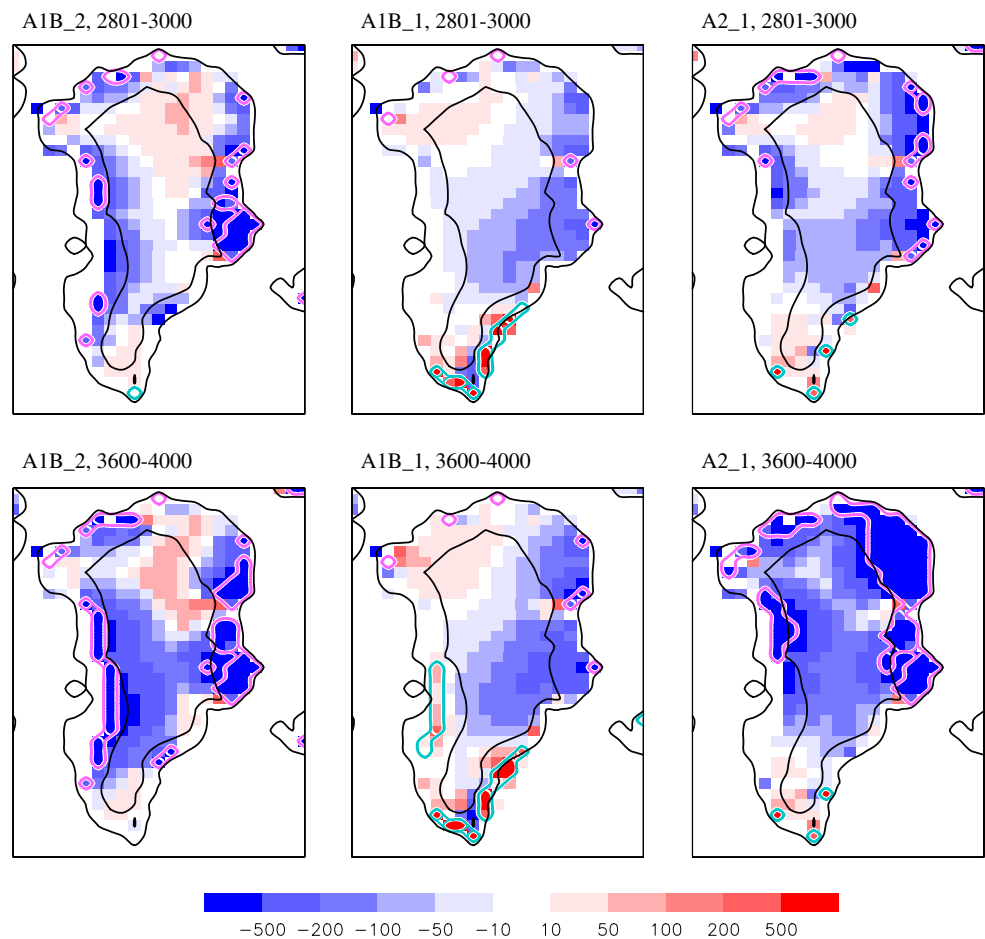
Fig. 16 Time series of different contributions to global mean sea level rise. **a** Northern hemisphere ice sheets, **b** Antarctic ice sheet, **c** global mean thermal expansion of sea water, **d** total global mean sea level rise. Units are m. For the colours of the individual experiments, see Fig. 11. Note the non-constant scale of the *x*-axis!



Ice thickness at the south eastern tip of Greenland is growing slightly for elevations above 2,000 m due to stronger snowfall. The moderate warming, due to weakened pole ward heat transport in the North Atlantic, is too small to cause a substantial change in melting. On the western and eastern flanks of the ice sheet a few grid points become ice free. This pattern amplifies during the next 1,000 years with a strong reduction in ice thickness on the western, eastern, and northwestern margin of the ice sheet. In the east and the west, the ice sheet retreats by at least one grid point (80 km). In the centre of North Greenland, ice thickness is increasing by more than 50 m compared to present values. In southeast Greenland, the area with

increasing thickness is almost unchanged after the year 3000. In the A1B-off experiments, the patterns of ice thickness change differ significantly from the changes in the A1B-on experiments. At the end of this millennium the reduction in ice thickness is strongest at the eastern side of Greenland and almost negligible in West Greenland. In contrast to the A1B-on experiment, the main cause of the ice loss is not the enhanced melting, but the reduced snowfall due to the cooling associated with the collapse of the North Atlantic overturning. At the coast of South Greenland, the melting is strongly reduced causing a strong build up of ice. Here accumulation rates increase. The lower temperatures (partly due to the height effect) cause a

Fig. 17 Changes in ice thickness relative to the control run. *Top row* averaged for the years 2801–3000, *bottom row* averaged over the years 3600–4000. Results are shown for one A1B simulation with a non-collapsed NAMOC (A1B_2), one with a non-collapsed NAMOC (A1B_1) and for one A2 simulation (A2_1). Units are m. Changes in the ice mask relative to the control run are indicated by *encircling in pink* (ice sheet retreat) and *light blue* (ice sheet advance). Isolines of surface topography are plotted in *black*. Displayed are the contours for 0 (land/sea mask) and 2,000 m



higher fraction of the precipitation to fall as snow. Thousand years later, the pattern of surface mass balance is essentially unchanged, but with increased amplitudes. In West Greenland the ice sheet is even advancing. The increase of ice thickness in the western and southern margin of the ice sheet contributes to explain the relative small reduction of the ice volume seen in Fig. 16a.

In the A2 simulations the pattern of the changes in ice thickness is relatively similar to the A1B-on experiments. Except for southern Greenland, ice thickness decreases at almost all margins. In the eastern and central part of Greenland, reduced snowfall in the interior can explain the lowered thickness. This effect also plays a role near the margin of the ice sheet. In southern Greenland, increased precipitation rates over the whole area and low melting rates at the margins lead to larger ice thickness in elevated areas and at several locations the ice sheet is expanding. In the year 4000, the reduction in ice sheet thickness and extent is drastic. An exception is southern Greenland, where the thickness is almost identical to the thickness 1,000 years earlier.

The effect of the changes in ice sheets on the deep water formation must be expected to be relatively small. The additional freshwater input into the North Atlantic is, in all experiments, dominated by the signal from the changes in atmospheric moisture transports. The effect of the melting of the Greenland ice sheet is typically smaller by an order of magnitude. The total additional freshwater input into the Arctic and North Atlantic was 0.22 Sv at the end of the A2_1 experiment, compared to 0.02 Sv input from Greenland melting. This is confirmed by the results of the A2-NOICE experiment without interactive ice sheets, which behaves like the other A2 experiments (not shown). However, in the A1B experiments, which are close to a bifurcation point, the contribution of the melting ice sheets might have influenced the ocean circulation substantially. In stabilisation experiments with the present model Winguth et al. (2005) show that the inclusion of the effect of melt water from Greenland has little effect on the evolution of the NAMOC.

The Antarctic ice sheet is growing in all greenhouse simulations (see Fig. 16b). The accumulation in the interior is dominating over enhanced melting at

the coasts. It must be noted that the model does not include an adequate treatment of ice shelves. A potential disintegration of the West Antarctic Ice Sheet due to a grounding line retreat caused by enhanced basal melting on the ice shelves due to warmer ocean temperatures (Warner and Budd 1998), cannot be simulated. Other potentially important processes that cannot be modelled with the present model are, e.g. basal lubrication due to the transport of surface water from summer melt through crevasses to the bottom of the ice sheet (Zwally et al. 2002). The control run is showing a slight drift of 0.2 m SLE in 1,000 years. After the year 2200, the increase in volume is almost linear in all experiments. In the A2 experiments, the volume has increased by 3.2 m SLE. In the A1B experiments, the increase lies between 2 and 2.2 m SLE and in the B1 experiment at 0.7 m SLE. A more detailed analysis will be given elsewhere (Vizcaíno 2006).

Ridley et al. (2005) performed a $4 \times \text{CO}_2$ experiment, where HadCM3 was bi-directionally coupled to a three-dimensional model of the Greenland ice sheet. After 1,000 years, the Greenland ice sheet is reduced to 40% of the initial volume. After 3,000 years, it is reduced to 4% of its original value. The melt water has only a small effect on the NAMOC. Maximum sea-level rise rates (5.5 mm year^{-1}) are reached over the first 300 years. Greve (2000) performed several 1,000-year simulations with the uncoupled three-dimensional ice sheet model SICOPOLIS and got a moderate reduction to 90% of the initial volume of the Greenland Ice Sheet for a uniform mean annual temperature increase of 3 K; and almost complete disintegration (7 m SLE) for the most extreme scenario with an assumed warming of 12 K. Alley et al. (2005) obtained sea level rises of 1, 2, and 3 m after 1,000-year simulations with the model from Huybrechts and de Wolde (1999) for the uniform increase in mean annual temperature, which was obtained from an average of seven IPCC models, in which the atmospheric CO₂ stabilises at 550, 750, and 1,000 ppm, respectively. Fichet et al. (2003) report a strong influence of the Greenland ice sheet melt water discharge on the NAMOC until the year 2100, although the simulated melt water from Greenland fluxes are comparable to the melting rates obtained with our model (0.015 Sv). However, their control run did show a considerable drift towards a weaker NAMOC. It cannot be excluded that this result is affected by the model drift or that their model is rather close to a bifurcation point of the NAMOC, where even marginal changes in meltwater input can cause a large impact.

Church et al. (2001) predict up to the year 2100 a continuous growth of the Antarctic ice sheet, compensating enhanced run-off from Greenland. Simulations with a two-dimensional climate model coupled to a three-dimensional ice sheet model by Huybrechts and de Wolde (1999) show a moderate and constant lowering of sea level, reaching 30 and 50 cm by the year 3000 for $2 \times$ and $4 \times \text{CO}_2$ experiments. In an $8 \times \text{CO}_2$ scenario, the contribution to sea level rise is positive, due to increased surface melting in the margins and to the effect of a warming ice shelf. Warner and Budd (1998) and Huybrechts and de Wolde (1999) showed that grounding line retreat along the major ice-shelves could happen for basal melting rates $>5\text{--}10 \text{ m year}^{-1}$, demising the West Antarctic Ice Shelves after a few centuries.

Until the year 3000, the thermal expansion of sea water leads to an increase of global mean sea level of about 2 m in the A2 experiments, 1 m in the A1B runs, and 0.25 m in the B1 runs (Fig. 16c). In the A1B-off simulations, the onset of convection in the North Pacific cools the ocean. This leads to a halving of the thermal expansion in these experiments until the year 4000 and a slow decrease afterwards.

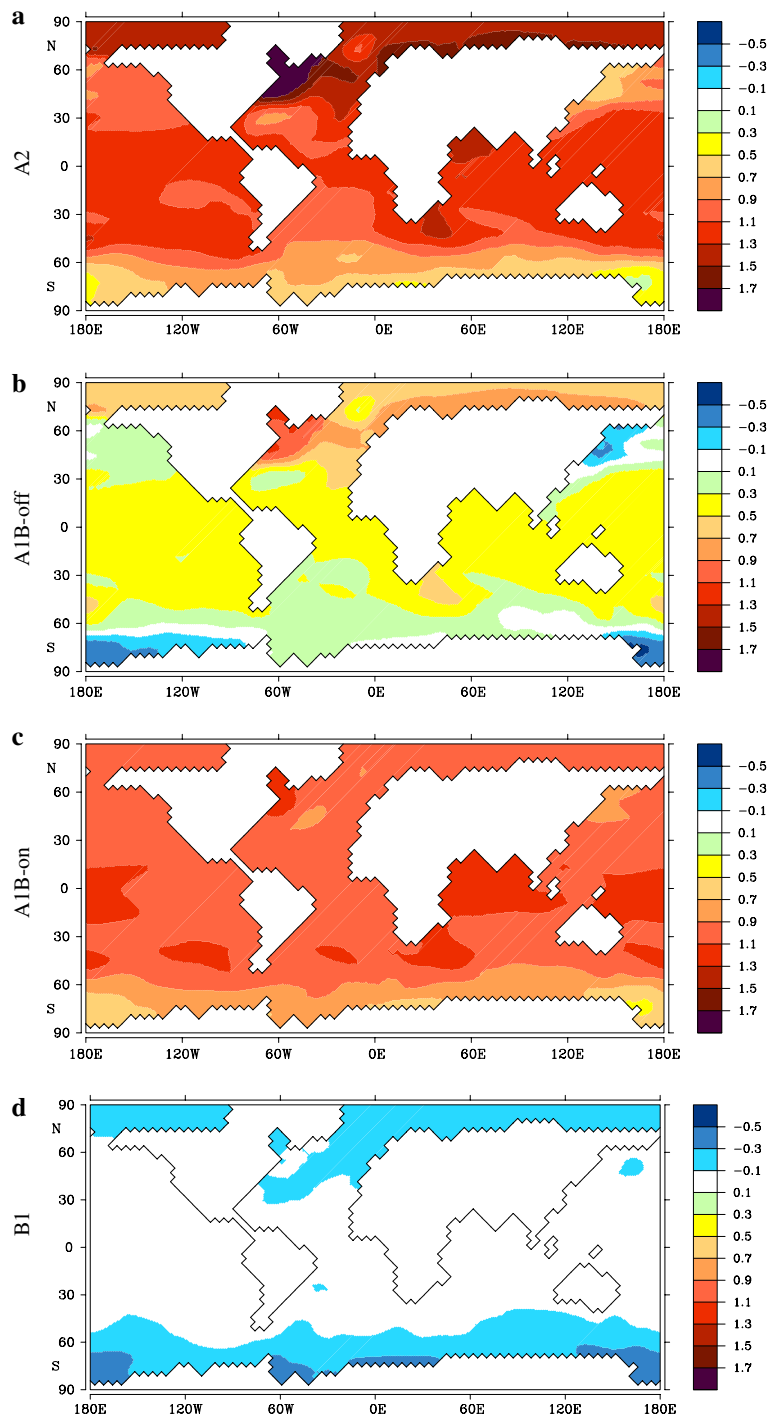
Figure 16d illustrates an unexpected change in global mean sea level. In the A2 simulations, global mean sea level rise peaks at roughly 0.9 m around the year 2700. For the remainder of these simulations, the global mean sea level is slowly decreasing leading to 0.5 m of global sea level rise in the year 5000. In the A1B-on simulations the peak of 0.8 m is reached around the year 3000. Between the years 3500 and 4000, the sea level is falling rapidly due to the dominance of the growth of the Antarctic ice sheet. In the year 4000, the sea level is approximately 0.4 m higher than in the control run. Thereafter the changes are rather small. In the A1B-off simulations, the peak of 0.4 m is reached in the year 2500, thereafter global mean sea level is sinking. In the year 4000, it is 1.5 m lower than in the control run due to the growth of the Antarctic ice sheet. The net change in global mean sea level in the B1 simulations is much smaller than in the other CO₂ experiments.

The spatial distribution of sea level change at the end of this millennium (averaged over the years 2801–3000) is very different between the experiments (see Fig. 18). The A2 experiments show a sea level rise everywhere. Maximum sea level rise is simulated in the northern North Atlantic and in the Arctic, where the collapse of the deep water formation and the stable stratification lead to a local sea level rise of typically 1.5 m. Maximal values of 1.8 m are simulated in the Labrador Sea. In the northwest Pacific, the convection

down to 2,000 m causes a minimum of sea level rise of 0.6 m. Common to all experiments, the lowest sea level rise can be seen around Antarctica. This is a consequence of the shift of the locations of convection. The spatial pattern in the A1B-off simulations is very similar, but the global mean value is substantially lower. This can be explained by the similarity of the changes in ocean circulation. The distribution of sea level

change in the A1B-on simulations is quite different: The amplitude of regional differences of sea level change is smaller due to the smaller changes in ocean circulation relative to the control simulation. Relatively high sea level rise is simulated in the Labrador Sea (reduced NADW formation) and in low latitudes. Minimal sea level rise is simulated at the coast of Antarctica and in the northwest Pacific, the latter

Fig. 18 Distribution of sea level change averaged over the years 2801–3000 for A2, A1B_on, and A1B_off ensembles. Displayed is the anomaly relative to the climate of the CTRL simulation. Only dynamically active grid points are displayed. Units are m



associated with a slight amplification in intermediate water formation.

3.2.5 Carbon cycle

During the first centuries of all greenhouse experiments, when the prescribed anthropogenic emissions are strong, both ocean and terrestrial biospheres take up anthropogenic carbon at comparable rates (see Fig. 19). Initially, the terrestrial uptake is even slightly larger (see Sect. 3.1). After the peak in atmospheric CO₂ concentrations has been passed, the amount of carbon stored in the terrestrial biosphere levels off and even starts to decrease slowly. Until the end of the experiments, the carbon content in the ocean continues to increase in all greenhouse experiments. At the year 4000, the increase in oceanic carbon content is 2,540 Pg C (A1B), 3,930 Pg C (A2), and 1,395 Pg C (B1). The differences between the individual realisations of the A1B simulations are relatively small, indicating that the strong changes of the MOC are relatively unimportant. The numbers for the carbon uptake of the terrestrial biosphere are 710 Pg C (A1B), 1,025 Pg C (A2), and 360 Pg C (B1). In the year 4000, the fraction of emitted carbon that remains in the atmosphere increases substantially with increasing emissions: Results range from 11% for the B1_1 simulation up to 25% for the A2_1 experiment. However, especially for the high emission scenario A2, equilibrium is not yet reached in the year 4000 and the ocean still takes up approx. 0.3 Pg C year⁻¹ with the long time constant of the deep circulation. Almost all of this carbon stems from the atmosphere; the terrestrial carbon storage is relative close to equilibrium.

The changes in ocean climate and circulation have a marked impact on the export production in the ocean (see Fig. 19d). From the year 2000 onwards, all CO₂ experiments show a marked reduction in export production similar to the results of previous studies (e.g. Maier-Reimer et al. 1996). In the A2 experiments, the total export production is reduced by 30% in the year 2500. The main reason for this reduction in productivity is the reduced nutrient availability in the euphotic zone. Due to the surface warming, the deep ocean has become stagnant. The nutrient content in the deep ocean increases due to the accumulation of particulate organic matter from the surface and the reduced exchange with the upper ocean. The consequence is a nutrient depletion of up to 30% in the upper 1,055 m (see Fig. 19e). A similar effect has been discussed in more detail in the paper of Winguth et al. (2005), analysing experiments with prescribed CO₂ concentrations. Towards the end of the experiments, in

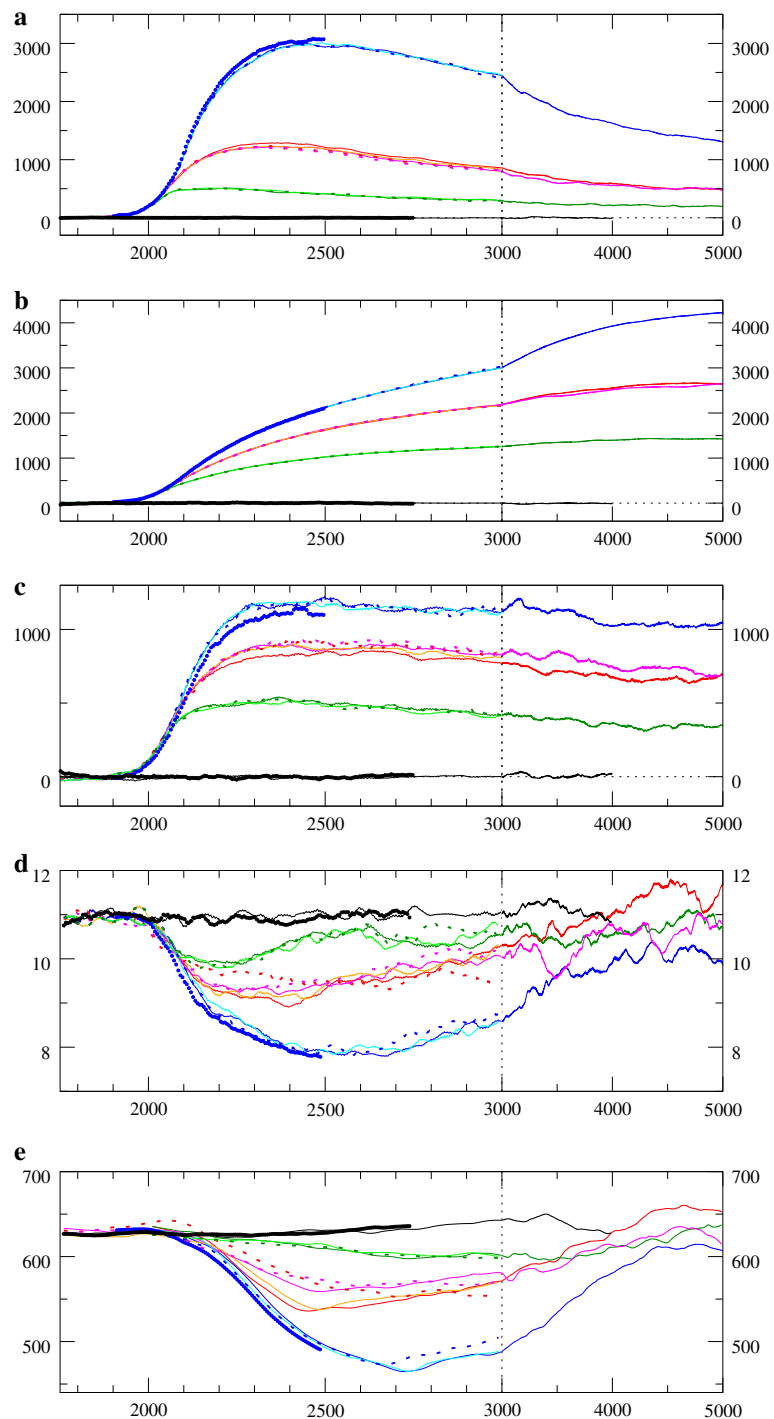
all cases, the export production intensifies again. Whereas in the B1 and A1B a similar level as in the control run is reached, the high emission scenario A2 does not recover to more than 90% of the control run level up to the year 5000, which is a consequence of the substantial changes in ocean circulation. A two-dimensional analysis of the changes in export production (not shown) indicates a pole ward shift of the production maxima at high latitudes due to warmer SSTs. The reduction is strongest where the production is strongest, especially in the upwelling zone of the equatorial Pacific, where the export production is reduced in spite of enhanced wind-driven upwelling.

The change in vertically integrated carbon for both land and ocean at the end of this millennium is shown in Fig. 20. Carbon content increases almost everywhere, except for some land areas in the mid-latitudes of the Northern Hemisphere. Here, warmer temperatures enhance respiration. The reduced soil carbon locally leads to a decrease of the total carbon content. The simulated large increase in carbon content in all scenarios for the regions north of 60°N is caused by a pole ward shift of the boreal forest due to warmer temperatures. Forest expansion can be seen as well for the African and Indian monsoon regions, Australia, and drier areas in North and South America. Only some regions around the Mediterranean show a decrease in vegetation cover, because precipitation decreases here.

The increase of carbon content in the terrestrial biosphere is mainly caused by the increased atmospheric CO₂ concentration. Off-line experiments with the climate data of these experiments show that climate change has a negative effect on carbon storage due to an increase in respiration in large areas, as was reported in other coupled models (e.g. Cox et al. 2000; Friedlingstein et al. 2001; Govindasamy et al. 2005; Fung et al. 2005). However, in contrast to Cox et al. (2000), on a global scale, the increased storage due to CO₂ increase in our model always dominates the decrease due to climate change. More details about the simulated vegetation changes and the terrestrial carbon storage can be found elsewhere (Schurgers 2006).

The carbon content in the ocean increases strongest in the North Atlantic. The signature of bottom topography on the amount of carbon storage is obvious, at least in the Atlantic. This indicates that the entire water column is exposed to higher carbon content. Three main mechanisms are contributing to the carbon enrichment in the deep ocean: (1) physical transport (advection, convection, mixing) of surface waters that are highly enriched with anthropogenic carbon (including changes of the solubility pump); (2)

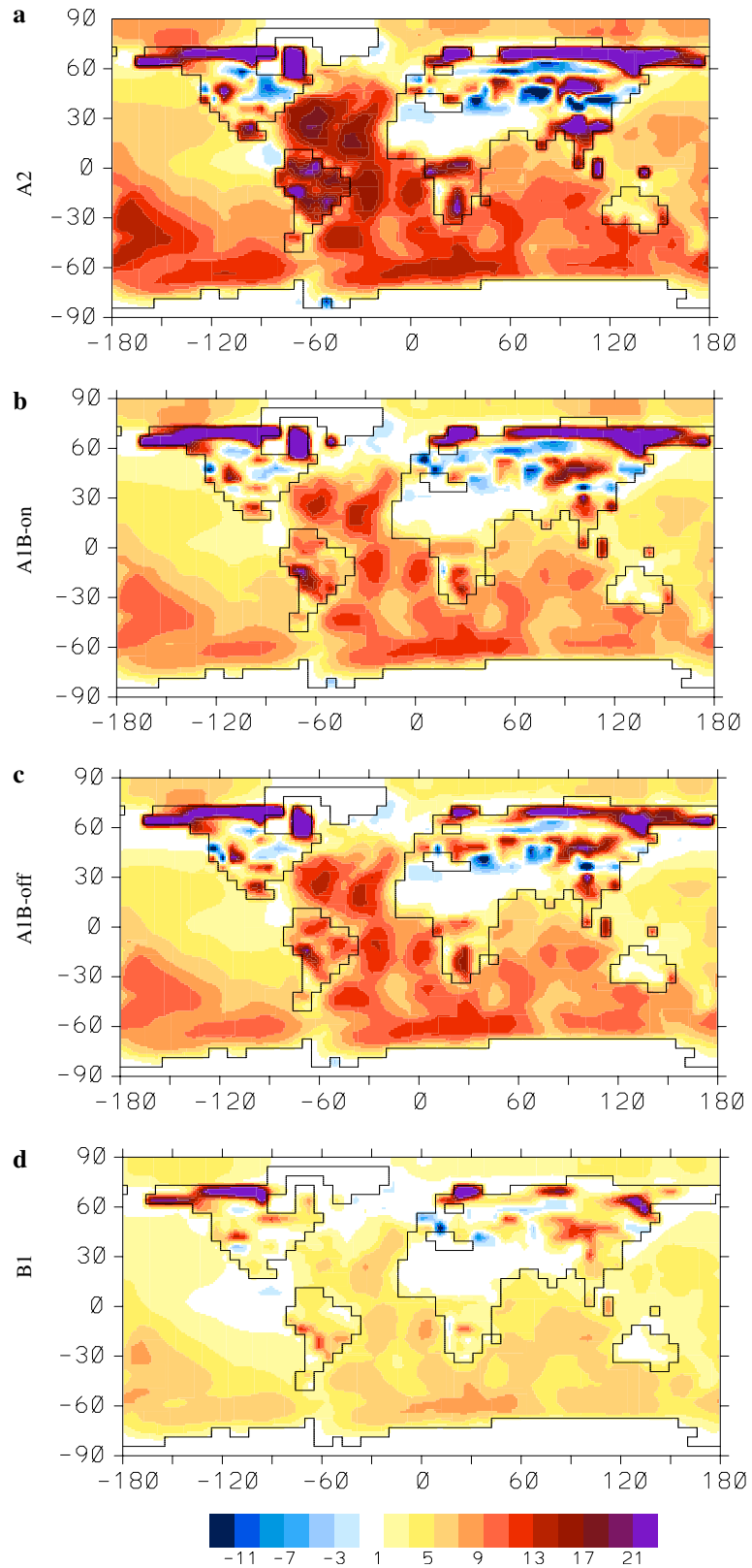
Fig. 19 Time series of change of carbon content in atmosphere (a), ocean (b), and land (c) compared to the climate of the control run.. Units are Pg C. The panels show global export production (d) (in Pg C year⁻¹) and phosphate content (e) in the upper 1,055 m of the model in 10¹² mol. For the colours of the individual experiments, see Fig. 11. Note the non-constant scale of the x-axis!



accumulation of particulate organic matter and CaCO₃ shells sinking down from the surface ocean, and (3) dissolution of marine sediments due to the more acidic water. In the simulations without collapse of the NADW formation, the first process dominates in the North Atlantic. In the simulations with a collapsed NAMOC cell, the deep waters of the North Atlantic transform from a low nutrient/high oxygen water mass

into an oxygen depleted water mass enriched with remineralised carbon and nutrients. In the A1B experiments, the difference between the simulations with and without collapse of NADW formation is comparably small (compare Fig. 20b, c). The amount of calcium carbonate in the sediment is reduced due to dissolution caused by more acidic conditions in the overlying water masses.

Fig. 20 Anomalies in the vertically integrated carbon content for A2 (a), A1B_on (b), A1B_off (c), and B1 (d). Units are kg C/m², data are averaged over the years 2801–3000. The oceanic data include changes in the sediment



Another maximum of oceanic carbon uptake is associated with formation of subsurface water masses around Antarctica. In the North Pacific, oceanic carbon

uptake is relatively small or even slightly negative. The deep water masses here show already in the control simulation a high enrichment with nutrients and

biogenic carbon. The amount of anthropogenic carbon being advected to these regions with the newly formed AABW is relatively small. The convection to intermediate depths in the A2 and the A1B-off experiments has mixed anthropogenic carbon down and brought carbon enriched mid-depth water in contact with the atmosphere, with respect to vertically integrated carbon both effects largely cancel each other. The minimum of carbon uptake in the tropical eastern Pacific is a consequence of the aforementioned strongly reduced biological production in this area. This results both in reduced accumulation of biogenic carbon and particulate organic carbon underneath as well as less accumulation of organic sediment. The warmer surface temperatures decrease the solubility of CO₂ in the surface waters. Thus, in both the A2 and the B1 simulations, the amount of carbon contained in these ocean grid points is somewhat smaller than in the control run (by up to 1 kgC/m²).

4 Summary and conclusions

A new earth system model consisting of the atmospheric GCM ECHAM3, the ocean GCM LSG2, the three-dimensional ice sheet model SICOPOLIS, the marine biogeochemistry model HAMOCC3, and the dynamic vegetation model LPJ was introduced. Some important quantities of the model climate were compared to observations. A modified version of the periodically-synchronous coupling technique was introduced and it was shown to work successfully. Due to the resulting reduction in computational cost, it is possible to perform long-term simulations of several thousand years with a GCM-type earth system model which hitherto have been performed with models of intermediate complexity only.

The earth system model was forced with three different anthropogenic CO₂ emission scenarios covering the years 1751–3000. The scenarios follow the IPCC emission scenarios B1, A1B, and A2, with an exponential decay with a time constant of 150 years after the year 2100. For each of these scenarios, an ensemble of simulations was performed. Individual simulations have been continued for another 2,000 years.

At the end of this millennium, the model simulates increased atmospheric CO₂ levels (416, 665, and 1,416 ppm). The atmospheric CO₂ concentrations are, at this time, slowly sinking due to negligible emissions and ongoing oceanic carbon uptake. The climate changes strongly reduce the ability of ocean and terrestrial biosphere to take up anthropogenic carbon. Thus, the atmospheric CO₂ concentrations obtained in

the year 3000 for the A2 scenario with and without climate change are 1,416 and 969 ppm.

The model simulates, at the end of the millennium, a global mean warming of 1.3, 3.0, and 4.9 K for the three scenarios. The simulated atmospheric moisture transports display enhanced convergence in the North Atlantic. As a consequence, the NAMOC shows, in all simulations, at least a temporal weakening. In the high emission scenario A2, the NAMOC collapses without any sign of recovery until the year 5000. The A1B scenario brings the model very close to the bifurcation point, with the NAMOC in three out of five simulations collapsing. 4 × CO₂ experiments with atmosphere–ocean GCMs also show either a complete collapse of deep water renewal (e.g. Manabe and Stouffer 1994) or only a reduced ventilation of the deep ocean (e.g. Voss and Mikolajewicz 2001a). Thus, the predictions made on this aspect might be highly model dependent, and it cannot be excluded that the flux correction for freshwater fluxes applied in this model might lead to a distortion of the bifurcation diagram.

Whereas the warming pattern in the simulations with non-collapsing NAMOC is rather similar to the results obtained from other models (stronger warming over land than over ocean, maximum warming in high northern latitudes, moderate warming in the northern North Atlantic and in the Southern Ocean), the simulations with a collapsed NAMOC lead to a substantial cooling over the northern North Atlantic with some extension to the north western European coasts.

For the Greenland ice sheet, the model simulated a decrease in volume. This result is independent of the choice of the emission scenario. The simulated melting rates are, however, typically one order of magnitude smaller than the additional freshwater input into the North Atlantic due to changes in atmospheric moisture transport. It is unlikely that they are the main driver of the collapse of the NAMOC, but in the A1B simulations, which are close to the bifurcation point of the system, they could have been important. The volume of the Antarctic ice sheet increases in all simulations. The increase in accumulation in the interior due to enhanced snowfall is stronger than the contribution of enhanced melting near the coast. However, as the ice sheet model does not include an adequate treatment of the physics of ice shelves, a potential collapse of the West Antarctic ice sheet could not be simulated properly. The climate sensitivity of the atmosphere model is relatively low. With a model with higher climate sensitivity, the simulated warming over Greenland most likely would have been higher, leading to higher melting rates.

For the next 500 years, the model predicts an increase of global mean sea level of up to 1 m. The dominant effect is the thermal expansion of the ocean. At least for the next 500 years, the contributions from the Greenland and Antarctic ice sheets largely cancel each other. In the year 4000 the changes in global mean sea level relative to the control run scatter between plus and minus 1.5 m. The collapse of the NAMOC leads to a drastic reduction in Greenland melting, and thus to an essential negative contribution of the cryosphere to sea level rise dominated by the enhanced accumulation over Antarctica. This also represents a stabilising feedback for the NAMOC. In a warmer climate, two partially compensating feedbacks modifying the freshwater input into the North Atlantic act on a collapsing NAMOC: An enhanced convergence of atmospheric moisture transport and a reduction of the melt water input from the Greenland ice sheet.

On longer time scales, the ocean is dominating the uptake of anthropogenic carbon. Carbon content on land increases, mostly due to the CO₂ fertilisation effect. Warming leads to enhanced growth of boreal forests in the north and enhances respiration of soil carbon. The reduced ventilation of the deep ocean leads to an accumulation of both nutrients and biogenic carbon in the deep ocean linked with reduced biological production (by up to 30%) due to reduced availability of nutrients in the euphotic zone. The reduced ventilation of the deep ocean as well as the collapse of the NAMOC lead to reduced downward physical transport of anthropogenic carbon, but also to less upward transport of nutrient rich, high CO₂ and low oxygen waters. As a result of these compensating effects, even the two-dimensional distribution of vertically integrated additional carbon content reacts relatively insensitive on a collapse of the NAMOC.

Climate change strongly reduced the ability of both ocean and land to sequester anthropogenic carbon. Thus, the simulated increase in atmospheric CO₂ concentrations was up to 44% higher in comparison to simulations neglecting the effect of climate change on the carbon cycle.

Especially on time scales of several centuries and longer, feedbacks between compartments not represented in atmosphere–ocean GCMs, which are the traditional tools of climate research, become increasingly important. Studies of long-term effects of anthropogenic emissions of greenhouse gases will require the use of earth system models including ice sheets, cycles of carbon and probably other elements.

The model simulations indicate the existence of an important bifurcation point in the earth system. The most likely SRES emission scenario, A1B, leads, in

some cases, to a collapse of the NAMOC with a cooling over the North Atlantic; the higher emission scenario A2 leads in all cases to a collapse of the NAMOC. Interbasin atmospheric moisture transports represent a feedback weakening the present mode of thermohaline circulation. The simulated weakening of the NAMOC in a typical IPCC setup until the year 2100 was rather moderate. This calls for comparable experiments with more models, in order to estimate the likelihood of potentially crossing the threshold of irreversible climate changes. The warming caused by the anthropogenic CO₂ emissions is an almost permanent feature and the cooling process after the peak CO₂ concentrations have been reached is a very slow process with time scales much longer than 1,000 years.

Acknowledgments This work was performed in the project CLIMCYC, funded by the DEKLIM program of the German Ministry of Education and Research. Arne Winguth is supported by NASA grant NAG5-11245 and the UW Graduate School Research Funds. The simulations have been performed at the “Deutsches Klimarechenzentrum”. Comments by Erich Roeckner, Matt Howard and two anonymous reviewers helped to improve the paper substantially. Norbert Noreiks helped to prepare the figures.

5 Appendix 1: Periodically synchronous coupling technique

During the synchronous simulation periods the air sea coupling coefficient α_0 is calculated as a function of sea ice thickness and sign of the heat flux according to

$$\alpha_0 = \begin{cases} 30 \text{ Wm}^{-2}\text{K}^{-1} & \text{in case of surface melting/absence of sea ice} \\ \text{for all other cases} & \min\left(30, \frac{2 \text{ m}}{0.0666667 \text{ m} + H_{\text{ice}}}\right) \text{ Wm}^{-2}\text{K}^{-1} \end{cases} \quad (3)$$

The net air–sea heat flux F_{h0} and the surface temperature of the ocean T_0 are stored daily for all grid points additionally to mass and momentum fluxes. For simplicity we introduce like Rahmstorf and Willebrand (1995) an effective restoring temperature T^* such that

$$F_{\text{h0}} = \alpha_0 (T^* - T_{0,\text{old}}) \quad (4)$$

In the ocean only periods a new effective coupling coefficient α_n is calculated from Eq. 3 using actual ice

thickness H_{ice} and air–sea heat flux F_{h0} . A perturbation atmospheric temperature T_a is introduced:

$$c_a \delta T_a / \delta t = -\lambda T_a + A_h \Delta T_a - \alpha_{0,\text{new}} T_a - ((\alpha_{0,\text{new}} - \alpha_{0,\text{old}}) T^* - \alpha_{0,\text{new}} T_{0,\text{new}} - \alpha_{0,\text{old}} T_{0,\text{old}}), \quad (5)$$

where $c_a (=3 \times 10^6 \text{ Wsm}^{-2} \text{ K}^{-1})$ represents the effective heat capacity of the lower troposphere. The first term on the right hand side is a linear damping with a coefficient of $2 \text{ Wm}^{-2} \text{ K}^{-1}$ representing the weak radiative negative feedback on large-scale surface temperature anomalies. The horizontal exchange is entirely diffusive with a diffusion constant A_h of $2.5 \times 10^6 \text{ m}^2/\text{s}$. The third term represents the heat loss of the anomalous air temperature to the ocean. The bracket assembles terms stemming from anomalies in the air–sea heat flux due to changes in ocean conditions relative to the conditions where the original heat flux has been calculated. The values follow Stone and Miller (1980). The behaviour of this equation has been discussed in detail in Marotzke and Pierce (1997). Equation 5 for T_a is solved implicitly. The freshwater and momentum fluxes from the previous synchronous integration periods are used without further modifications.

Using the forcing of only 1 year repeatedly would lead to a strong model drift in the ocean only periods due to rectification processes and to an unrealistic variability in the ocean due to the ocean being exposed for a long time to anomalies stemming from interannual variability. In order to represent both the mean climatological forcing and its variability reasonably well, several years of data have to be used repeatedly. Whereas the representation of the mean and variability becomes better with increasing number of years, this introduces an artificial delay in case of changing climate, too. Experiments showed that an archive length of 8 years seems to be the minimum length in order to obtain an acceptable approximation of the mean climate and variability without large artificial model drift in the ocean-only simulation periods.

Two different approaches have been used for the length of the ocean-only periods. The simplest approach uses fixed lengths of the synchronous and ocean-only periods. In this paper, we used alternating periods of two synchronous years and eight ocean-only years. Compared to the fully coupled model this is 4.7 times faster. An alternative approach yielding an even higher reduction in computer time involves an interactive calculation of the length of the ocean-only period from the actual state of the ocean. The model is switched into the fully synchronous mode with atmospheric GCM only when SST and sea ice properties are very different than the

ones used for calculation of the atmospheric forcing. As this involves a yes/no decision for a rather complex problem, thus some subjectivity is unavoidable. The anomalous air–sea heat flux is used for calculating this criterion. The quantity chosen to calculate is a global mean of the squared anomalous heat flux. If the sum over the time since the beginning of the ocean-only period, where older values are discarded with an e-folding time of 1 month, exceeds a cut off value (in this study: $3,600 \text{ W}^2\text{m}^{-4}$), the surplus is added to a final cut off criterion. If this exceeds another predefined cut off value (in this study: $360 \times 360^2 \text{ W}^2\text{m}^{-4}$), the ocean-only integration is stopped and the atmospheric forcing is calculated again interactively by the atmospheric GCM. The second variable was introduced in order to guarantee that only long-term mismatches in ocean surface conditions lead to a stop of the ocean-only integrations and to make the response function more stiff. This approach allows to choose the weighting between the potential inaccuracies and artificial delays and the required computer time. In any case, strong changes in air–sea heat flux, especially at the sea ice edge, switch the mode of integration and the atmospheric GCM is switched on more often. Ocean-only periods without substantial change in oceanic surface conditions can reach a predefined maximal length (48 years in this study).

For the land vegetation model LPJ and for the ice sheet model SICOPOLIS a similar approach is adopted, but the decision for a potential end of the simulation period without atmospheric GCM is made in the ocean model. During the periods of fully interactive coupled simulations, atmospheric forcing data for LPJ and SICOPOLIS are stored and used during the subsequent simulation periods where the ocean is driven by an energy balance model.

The validity of this method has been tested by repeating some simulations with a fully synchronously coupled model. The results are discussed in Appendix 2.

6 Appendix 2: Synchronous versus periodically synchronous coupling

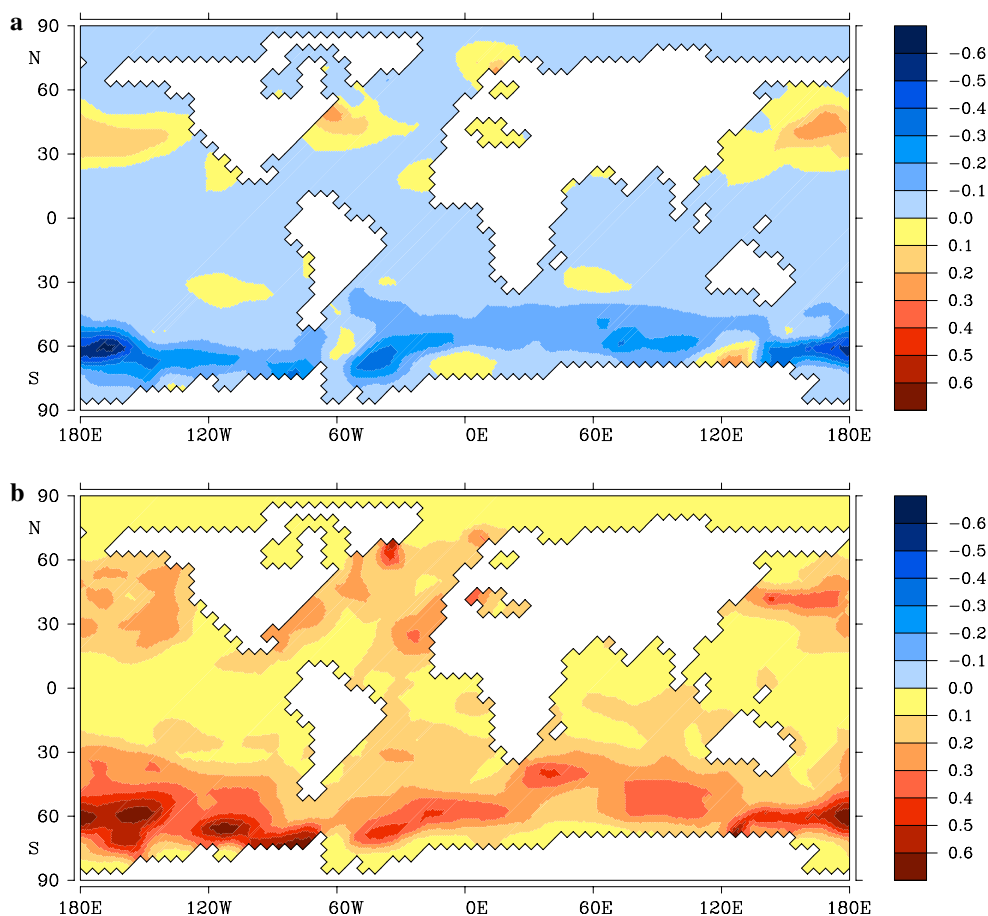
In order to be useful, the periodically synchronous coupling technique has to reproduce the climate of a fully synchronous integration, and it should only have a small effect on the transient behaviour of the coupled system. The climate of the 1,000-year fully-synchronous integration CTRLS differs only marginally from the climate of the 2,250 periodically-synchronous control integration CTRL. The difference in climate of the surface temperature between the two experiments is shown in Fig. 21a. Positive values of up to 0.2 K are

simulated in the northern subtropics; negative values with a peak value of 0.6 K in the Southern Ocean. These deviations are related to the long-term variations in the formation of AABW and the resulting changes of the MOC in the oceans. For comparison, the standard deviation of 1,000-year means of calculated from a 10,000 year long control run without interactive ice sheets is shown in Fig. 21b. The differences between the climates of the fully-synchronous and the periodically synchronous integrations exceed only in few places one standard deviation of the long-term variability. For the first 1,000 years of the synchronous and the periodically synchronous coupled simulations, the difference in the global mean SST is 0.01 K, but fluctuations of 1,000-year means in the 10,000-year integration with fixed ice sheets show peak to peak fluctuations of more than 0.15 K.

In order to test whether the periodically synchronous coupling technique induced any artefacts on the simulated climate signals, one part of experiment A2_1 was repeated with a fully synchronously integrated model. The simulation A2_1S covers the years 1901–2500, and thus the entire period with strong changes in

the surface conditions. Comparison of the different time series for the synchronous A2_1S integration and the periodically synchronous A2 simulations shows that the synchronous integration has very similar behaviour as the periodically-synchronously coupled integrations. This is true for all oceanic quantities like, e.g. global mean near surface air temperature, ocean heat uptake, and time series of meridional overturning (see Fig. 11). There is a slight delay introduced by the periodically synchronous coupling, especially for the collapse of the NAMOC. Whereas the forcing of temperature seems to work quite well with the energy balance treatment, there is a systematic delay in the application of changes in atmospheric moisture transports, as the data in the archive correspond to years with lower temperatures and CO₂ concentrations. As a consequence, the periodically-synchronous coupling leads to a delay of roughly two decades with respect to the response of the system to changes in atmospheric greenhouse gas composition, which can be seen most clearly in the biogeochemical components of the model (see Fig. 19a–c). The collapse of the NAMOC shows the same superimposed multidecadal oscillations for all

Fig. 21 **a** Difference in the climate of 1,000 year long synchronous control integration CTRLS and the periodically synchronous control integration CTRL. **b** Standard deviation of 1,000 year means from a 10,000 yearlong control integration with prescribed ice sheets. Units are K



A2 experiments, an indication that the dynamics of the transitions are treated adequately in the periodically-synchronous case.

The CO₂ concentration in the atmosphere in the periodically-synchronous simulations is slightly lower than the synchronous simulation (up to approximately 50 ppm around the years 2300–2500). For the periods without calculation of an atmospheric GCM in the periodically-synchronous coupling, the land vegetation model was forced with somewhat too low temperatures during the period of rapidly rising atmospheric temperatures (because of the forcing with climate data from the archive), and took up slightly too much carbon. A similar delay can be seen in the ice sheet model. However, the focus of this paper is on centennial to millennial scale changes and the bias from the coupling technique is, for most parameters, within the error bars set by natural variability. Thus, we conclude that the coupling technique is appropriate in order to address the objectives of this study.

References

- Alley RB, Clark PU, Huybrechts P, Joughin I (2005) Ice-sheet and sea-level changes. *Science* 310:456
- Bacon S (1997) Circulation and fluxes in the North Atlantic between Greenland and Ireland. *J Phys Oceanogr* 27:1420–1435
- Baumgartner A, Reichel E (1975) *Die Weltwasserbilanz*. Oldenbourg, München
- Bryden H, Roemmich DH, Church JA, (1991) Ocean heat transport across 24°N in the Pacific. *Deep Sea Res* 38:297–324
- Chevallier F, Bauer P, Kelly G, Jakob C, McNally T (2001) Model clouds over oceans as seen from space: comparison with HIRS/2 and MSU radiances. *J Clim* 14(21):4216–4229
- Church JA et al (2001) Changes in sea level. In: Houghton JT, Ding Y, Griggs DJ, Noguer M, Van Der Linden PJ, Dai X, Maskell K, Johnson CA (eds) *Climate change 2001: the scientific basis*. Cambridge University Press, Cambridge, pp 640–693
- Cox PM, Betts RA, Jones C, Spall SA, Totterdell IJ (2000) Acceleration of global warming due to carbon-cycle feedbacks in a coupled climate model. *Nature* 408:184–187
- Cramer W, Bondeau A, Woodward FI, Prentice IC, Betts RA, Brovkin V, Cox PM, Fisher V, Foley JA, Friend AD, Kucharik C, Lomas MR, Ramankutty N, Sitch S, Smith B, White A, Young-Molling C (2001) Global response of terrestrial ecosystem structure and function to CO₂ and climate change: results from six dynamic global vegetation models. *Global Change Biol* 7:357–373
- Dixon KW, Delworth TL, Spelman MJ, Stouffer RJ (1999) The influence of transient surface fluxes on North Atlantic overturning in a coupled GCM climate change experiment. *Geophys Res Lett* 26:2749–2752
- Dufresne J-L, Friedlingstein P, Berthelot M, Bopp L, Ciais P, Fairhead L, Le Treut H, Monfray P (2002) On the magnitude of positive feedback between future climate change and the carbon cycle. *Geophys Res Lett* 29. DOI 10.1029/2001GL013777
- Eppley RW (1972) Temperature and phytoplankton growth in the sea. *Fish Bull* 70:1063–1085
- Farquhar GD, Von Caemmerer S, Berry JA (1980) A biochemical model of photosynthetic CO₂ assimilation in leaves of C₃ species. *Planta* 149:78–90
- Fichefet T, Poncin C, Goosse H, Huybrechts P, Janssens I, Le Treut H (2003) Implications of changes in freshwater flux from the Greenland ice sheet for the climate of the 21st century. *Geophys Res Lett* 30:1911. DOI 10.1029/2003GL017826
- Foley JA, Prentice IC, Ramankutty N, Levis S, Pollard D, Sitch S, Haxeltine A (1996) An integrated biosphere model of land surface processes, terrestrial carbon balance, and vegetation dynamics. *Global Biogeochem Cycles* 10(4):603–628
- Friedlingstein P, Bopp L, Ciais P, Dufresne J-L, Fairhead L, LeTreut H, Monfray P, Orr J (2001) Positive feedback between future climate change and the carbon cycle. *Geophys Res Lett* 28:1543–1546
- Friedlingstein P, Dufresne J-L, Cox PM, Rayner P (2003) How positive is the feedback between climate change and the carbon cycle? *Tellus* 55B:692–700
- Fung IY, Doney SC, Lindsay K, John J (2005) Evolution of carbon sinks in a changing climate. <http://www.pnas.org/cgi/doi/10.1073/pnas.0504949102>
- Ganachaud A, Wunsch C (2000) Improved estimates of global ocean circulation, heat transport and mixing from hydrographic data. *Nature* 408:453–457
- Ganachaud A, Wunsch C (2003) Large-scale ocean heat and freshwater transports during the world ocean circulation experiment. *J Clim* 16:696–705
- Gent PR, Willebrand J, McDougall T, McWilliams JC (1995) Parameterizing eddy-induced tracer transports in ocean circulation models. *J Phys Oceanogr* 19:2962–2970
- Gibson JK, Källberg P, Uppala S, Hernandez A, Nomura A, Serrano E (1997) ERA description ECMWF Re-Anal Proj Rep Ser 1, Reading UK
- Gouretski VV, Koltermann KP (2004) WOCE global hydrographic technical report, Berichte des BSH Nr. 35, Hamburg 50 p, 2 CD-ROMs
- Govindasamy B, Thompson S, Mirin A, Wickert M, Caldeira K (2005) Increase of carbon cycle feedback with climate sensitivity: results from a coupled climate and carbon cycle model. *Tellus* 57B:153–163
- Gregory JM, Dixon KW, Stouffer RJ, Weaver AJ, Driesschaert E, Eby M, Fichefet T, Hasumi H, Hu A, Jungclaus JH, Kamenkovich IV, Levermann A, Montoya M, Murakami S, Navrath S, Oka A, Sokolov AP, Thorpe RB (2005) A model intercomparison of changes in the Atlantic thermohaline circulation in response to increasing atmospheric CO₂ concentration. *Geophys Res Lett* 32. DOI 10.129/2005GL023209
- Greve R (1997) Application of a polythermal three-dimensional ice sheet model to the Greenland ice sheet: response to steady-state and transient climate scenarios. *J Clim* 10(5):901–918
- Greve R (2000) On the response of the Greenland ice sheet to greenhouse climate change. *Clim Change* 46:289–303
- Holfort J, Siedler G (2001) The meridional ocean transports of heat and nutrients in the South Atlantic. *J Phys Oceanogr* 31:5–29
- Houghton RA, Hackler JL (2002) Carbon flux to the atmosphere from land-use changes. In: *Trends: a compendium of data on global change*. Carbon Dioxide Information Analysis Cen-

- ter, Oak Ridge National Laboratory, US Department of Energy, Oak Ridge, Tenn, USA
- Houghton JT, Ding Y, Griggs DJ, Nogueir M, Van Der Linden PJ, Dai X, Maskell K, Johnson CA (2001) Climate change 2001: the scientific basis. Cambridge University Press, Cambridge
- Huffman GJ, Adler RF, Arkin P et al (1997) The global precipitation climatology project (GPCP) combined precipitation dataset. *Bull Am Meteorol Soc* 78(1):5–20
- Huybrechts P, de Wolde J (1999) The dynamic response of the Greenland and Antarctic ice sheets to multiple-century climatic warming. *J Clim* 12:2169–2188
- Jickells TD, An ZS, Andersen KK et al (2005) Global iron connections between desert dust, ocean biogeochemistry and climate. *Science* 308(5718):67–71
- Jones PD, New M, Parker DE, Martin S, Rigor IG (1999) Surface air temperature and its variations over the last 150 years. *Rev Geophys* 37:173–199
- Jungclaus JH, Haak H, Esch M, Roeckner E, Marotzke J (2006) Will Greenland melting halt the thermohaline circulation? *Geophys Res Lett* (in press)
- Kalnay E et al (1996) The NCEP/NCAR 40-year reanalysis project. *Bull Am Meteorol Soc* 77(3):437–470
- Klein B, Molinari JB, Müller TJ, Siedler G, (1995) A transatlantic section at 14.5°N: meridional volume and heat fluxes. *J Mar Res* 53:929–957
- Latif M, Roeckner E, Mikolajewicz U, Voss R (2000) Tropical stabilisation of the thermohaline circulation in a greenhouse warming simulation. *J Clim* 13:1809–1813
- Lavin A, Bryden L, Parilla G (1998) Meridional transport and heat flux variations in the subtropical North Atlantic. *Global Atmos Ocean Syst* 6:269–293
- Macdonald AM, Wunsch C (1996) An estimate of global ocean circulation and heat fluxes. *Nature* 382:436–439
- Maier-Reimer E (1993) Geochemical cycles in an ocean general circulation model. Preindustrial tracer distributions. *Global Biogeochem Cycles* 7:645–677
- Maier-Reimer E, Mikolajewicz U, Hasselmann K (1993) Mean circulation of the Hamburg LSG OGCM and its sensitivity to the thermohaline surface forcing. *J Phys Oceanogr* 23:731–757
- Maier-Reimer E, Mikolajewicz U, Winguth A (1996) Interactions between ocean circulation and the biological pumps in the global warming. *Clim Dyn* 12:711–721
- Manabe S, Stouffer RJ (1988) Two stable equilibria of a coupled ocean atmosphere model. *J Clim* 1:841–866
- Manabe S, Stouffer RJ (1994) Multiple-century response of a coupled ocean-atmosphere model to an increase of the atmospheric carbon dioxide. *J Clim* 7:5–23
- Manabe S, Stouffer RJ (1997) Coupled ocean-atmosphere model response to freshwater input: comparison to Younger Dryas event. *Paleoceanogr* 12:321–336
- Marland G, Boden TA, Andres RJ (2005) Global, regional, and national fossil fuel CO₂ emissions. In: Trends: a compendium of data on global change. Carbon Dioxide Information Analysis Center, Oak Ridge National Laboratory, US Department of Energy, Oak Ridge, Tenn., USA
- Marotzke J, Pierce DW (1997) On spatial scales and lifetimes of SST anomalies beneath a diffusive atmosphere. *J Phys Oceanogr* 27:133–139
- Marsland SJ, Haak H, Jungclaus JH, Latif M, Röske F (2003) The Max-Planck-Institute global ocean/sea ice model with orthogonal curvilinear coordinates. *Ocean Model* 5(2):91–127
- Mikolajewicz U, Voss R (2000) The role of the individual air-sea flux components in CO₂-induced changes of the ocean's circulation and climate. *Clim Dyn* 16:627–642
- Mikolajewicz U, Crowley TJ, Schiller A, Voss R (1997) Modeling North Atlantic/North Pacific teleconnections during the Younger Dryas. *Nature* 387:384–387, plus erratum 388:602
- Nakicenovic N, Alcamo J, Davis G, De Vries B, Fenhann J, Gaffin S, Gregory K, Grübler A, Jung TY, Kram T, Lebre La Rovere E, Michaelis L, Mori S, Morita T, Pepper W, Pitcher H, Price L, Riahi K, Roehrl A, Rogner H-H, Sankovski A, Schlesinger M, Shukla P, Smith S, Swart R, Van Rooijen S, Victor N, Dadi Z (2001) Special report on emissions scenarios. A special report of Working Group III of the intergovernmental panel on climate change. Cambridge University Press, Cambridge
- Orr JC, Maier-Reimer E, Mikolajewicz U, Monfray P, Sarmiento JL, Toggweiler JR, Taylor NK, Palmer J, Gruber N, Sabine CL, Le Quere C, Key RM, Boutin J (2001) Estimates of anthropogenic carbon uptake from four three-dimensional global ocean models. *Global Biogeochem Cycles* 15(1):43–60
- Pacanowski RC, Philander G (1981) Parametrization of vertical mixing in numerical models of the tropical ocean. *J Phys Oceanogr* 11:1442–1451
- Petoukhov V, Ganopolski A, Brovkin V, Claussen M, Eliseev A, Kubatzki C, Rahmstorf S (2000) CLIMBER-2: a climate system model of intermediate complexity. Part I: model description and performance for present climate. *Clim Dyn* 16:1–17
- Petoukhov V, Claussen M, Berger A, Crucifix M, Eby M, Eliseev AV, Fichefet T, Ganopolski A, Goosse H, Kamenkovich I, Mokhov II, Montoya M, Mysak LA, Sokolov L, Stone P, Wang Z, Weaver AJ (2005) EMIC Intercomparison Project (EMIP): comparative analysis of EMIC simulations of climate, and of equilibrium and transient responses to atmospheric CO₂ doubling. *Clim Dyn* 25:363–385
- Rahmstorf S, Willebrand J (1995) The role of temperature feedback in stabilizing the thermohaline circulation. *J Phys Oceanogr* 25:787–805
- Reeh N (1991) Parameterization of melt rate and surface temperature on the Greenland Ice Sheet. *Polarforschung* 59(3):113–128
- Ridley JK, Huybrechts P, Gregory JM, Lowe JA (2005) Elimination of the Greenland ice sheet in a high CO₂ climate. *J Clim* 18:3409–3427
- Roeckner E, Arpe K, Bengtsson L, Brinkop S, Dümenil L, Esch M, Kirk E, Lunkeit F, Ponater M, Rockel B, Sausen R, Schlese U, Schubert S, Windelband M (1992) Simulation of the present-day climate with the ECHAM model: impact of the model physics and resolution. Max-Planck-Institut für Meteorologie, Hamburg, Report No 93
- Saenko OA, Schmittner A, Weaver AJ (2004) The Atlantic-Pacific Seesaw. *J Clim* 17:2033–2038
- Saunders PM, King BA (1995) Oceanic fluxes in the WOCE A11 section. *J Phys Oceanogr* 25:1942–1958
- Schiller A, Mikolajewicz U, Voss R (1997) The stability of the North Atlantic thermohaline circulation in a coupled ocean-atmosphere general circulation model. *Clim Dyn* 13:325–347
- Schmittner A, Latif M, Schneider B (2005) Model projections of the North Atlantic thermohaline circulation for the 21st century assessed by observations. *Geophys Res Lett* 32:L23710. DOI 10.129/2005GL024368
- Schmitz WJ (1995) On the interbasin-scale thermohaline circulation. *Rev Geophys* 33:151–173
- Schurgers G (2006) Long-term interactions between vegetation and climate—model simulations for past and future, vol 27. *Berichte zur Erdsystemforschung*, Hamburg, pp 143. Avail-

- able at <http://www.mpimet.mpg.de/wissenschaft/publikationen/erdsystemforschung.html>)
- Smith EL (1936) Photosynthesis in relation to light and carbon dioxide. *Proc Natl Acad Sci USA* 22:504–511
- Sitch S, Smith B, Prentice IC, Arneeth A, Bondeau A, Cramer W, Kaplan JO, Levis S, Lucht W, Sykes MT, Thonicke K, Venevsky S (2003) Evaluation of ecosystem dynamics, plant geography and terrestrial carbon cycling in the LPJ dynamic global vegetation model. *Global Change Biol* 9:161–185
- Speer KG, Holfort J, Reynard T, Siedler G (1996) South Atlantic heat transport at 11°S. In: Wefer G, Berger WH, Siedler G, Webb DJ (eds) *The South Atlantic: present and past circulation*. Springer, Berlin Heidelberg New York, pp 105–120
- Stone PH, Miller DA (1980) Empirical relations between seasonal changes in meridional temperature gradients and meridional fluxes of heat. *J Atmos Sci* 37(8):1708–1721
- Stouffer RJ, Manabe S, Bryan K (1989) Interhemispheric asymmetry in climate response to a gradual increase of atmospheric CO₂. *Nature* 342:660–662
- Stouffer RJ, Yin J, Gregory JM, Dixon KW, Spelman MJ, Hurlin W, Weaver AJ, Eby M, Flato GM, Hasumi H, Hu A, Jungclaus JH, Kamenkovich IV, Levermann A, Montoya M, Murakami S, Nawrath S, Oka A, Peltier WR, Robitaille DY, Sokolov A, Vettoretti G, Weber SL (2006) Investigating the causes of the response of the thermohaline circulation to past and future climate changes. *J Clim* 19:1365–1387
- Sweby PK (1984) High-resolution schemes using flux limiters for hyperbolic conservation-laws. *Siam J Num Anal* 21:995–1011
- Swingedouw D, Braconnot P, Marti O (2006) Sensitivity of the Atlantic meridional overturning circulation to the melting from northern glaciers in climate change experiments. *Geophys Res Lett* 33:L07711. DOI 10.1029/2006GL025765
- Talley LD, Reid JL, Robbins PE (2003) Data-based meridional overturning stream functions for the global ocean. *J Clim* 16(19):3213–3226
- Visbeck M, Marshall J, Haine T, Spall M (1997) Specification of eddy transfer coefficients in coarse resolution ocean circulation models. *J Phys Oceanogr* 27:381–402
- Vizcaíno M (2004) Adaptive changes in a 3-D ice sheet model for its use in palaeosimulations. Diplomarbeit Meteorologisches Institut der Universität Hamburg, unpublished manuscript
- Vizcaíno M (2006) Long-term interactions between ice sheets and climate under anthropogenic greenhouse forcing. Simulations with two complex earth system models, vol 30. *Berichte zur Erdsystemforschung* 30, Hamburg, pp 183. Available at <http://www.mpimet.mpg.de/wissenschaft/publikationen/erdsystemforschung.html>
- Volk T, Hoffert MI (1985) Ocean carbon pumps: analysis of relative strengths and efficiencies in ocean–river atmospheric CO₂ changes. In: Sunquist ET, Broecker WS (eds) *The carbon cycle and atmospheric CO₂: natural variations archean to present*. Geophys Monogr Ser vol. 32, AGU, Washington, pp 99–110
- Voss R, Mikolajewicz U (2001a) Long-term climate changes due to increased CO₂ concentration in the coupled atmosphere–ocean general circulation model ECHAM3/LSG. *Clim Dyn* 17:35–60
- Voss R, Mikolajewicz U (2001b) The climate of 6000 years BP in near-equilibrium simulations with a coupled AOGCM. *Geophys Res Lett* 28(11):2213–2216
- Voss R, Sausen R (1996) Techniques for asynchronous and periodically synchronous coupling of atmosphere and ocean models. Part II: impact of variability. *Clim Dyn* 12:605–614
- Voss R, Sausen R, Cubasch U (1998) Periodically synchronously coupled integrations with the atmosphere–ocean general circulation model ECHAM3/LSG. *Clim Dyn* 14:249–266
- Warner RC, Budd WF (1998) Modelling the long-term response of the Antarctic ice sheet to global warming. *Ann Glaciol* 27:161
- Watson RT, Noble IR, Bolin B, Ravindranath NH, Verardo DJ, Dokken DJ (2000) Land use, land use change and forestry. Special report, Intergovernmental Panel on Climate Change. Cambridge University Press, Cambridge
- Weaver AJ, Eby M, Wiebe EC, Bitz CM, Duffy PB, Ewen TL, Fanning AF, Holland MM, MacFadyen A, Matthews HD, Meissner KJ, Saenko O, Schmittner A, Wang HX, Yoshimori M (2001) The UVic earth system climate model: model description, climatology, and applications to past and future climates. *Atmos Ocean* 39(4):361–428
- Wijffels S (2001) Ocean transport of fresh water. In: Siedler G, Church J, Gould J (eds) *Ocean circulation and climate*. Academic Press, pp 475–488
- Winguth AME, Maier-Reimer E, Mikolajewicz U, Segschneider J (1994) El Niño–Southern oscillation related fluctuations of the marine carbon cycle. *Global Biogeochem Cycles* 8:39–63
- Winguth A, Mikolajewicz U, Gröger M, Maier-Reimer E, Schurgers G, Vizcaíno M (2005) Centennial-scale interactions between the carbon cycle and anthropogenic climate change using a dynamic earth system model. *Geophys Res Lett* 32(23):L23714. DOI 10.1029/2005GL023681
- Wright DG, Stocker TF (1993) Younger Dryas experiments. In: Peltier WR (ed) *Ice in the climate system*. Springer, Berlin Heidelberg New York, pp 395–416
- Xie PP, Arkin PA (1997) Global precipitation: a 17-year monthly analysis based on gauge observations, satellite estimates, and numerical model outputs. *Bull Am Meteorol Soc* 78(11):2539–2558
- Zwally H, Abdalati W, Herring T, Larson K, Saba J, Steffen K (2002) Surface melt-induced acceleration of Greenland ice-sheet flow. *Science* 297:218–222